Diplomarbeit

Simulation of the Flow Through Nanopores

Ausgeführt am Institut für

Analysis und Scientific Computing

der Technischen Universität Wien

unter der Anleitung von

Associate Prof. Dr.techn.

Dipl.-Ing. Clemens Heitzinger

durch

Andreas Buttinger-Kreuzhuber

Lilienbrunngasse 3/10, 1020 Wien

Wien, 9. Dezember 2015

ABSTRACT

The work at hand deals with the simulation of flow in nanopores. Nanopores may serve as the ultimate tool for analyzing DNA and biomolecules due to their label-free single-molecule approach. This thesis aims at providing an efficient numerical approach and simulations to yield a better understanding of the physics inside nanopores and hence enable rational design.

The model is based on a steady-state continuum model, namely the Poisson-Nernst-Planck-Stokes (or drift-diffusion-Stokes-Poisson) system. Since boundary and interface conditions are not straightforward, they are discussed explicitly.

The computational method for solving the system of partial differential equations relies on the finite element method. An efficient numerical approach was developed in order to increase accuracy of the solutions while keeping memory requirements and computational time low. The approach involves a modified Newton's method and adaptive mesh refinement. Due to the axisymmetric nature of nanopores, most simulations are performed in cylindrical coordinates. The implementation is based on the free software package FEniCS to be capable of steering the numerical solution process.

In order to validate the modeling approach and to gain further insights into the physics, simulations are performed. Two state-of-the-art nanopores are examined in detail, a small DNA origami and a larger solid-state nanopore. The focus lies on simulations of the forces acting on molecules and on reproducing current-voltage curves. Current simulations indicate that physical parameters have to be carefully examined inside the pore so that simulation and experiment agree. Furthermore, simulations of the forces acting on a molecule are presented and compared with forces calculated under the assumption of a point-like molecule. A force field is shown to demonstrate the possibility of a comprehensive simulation of nanopores as stochastic sensors.

ZUSAMMENFASSUNG

Die vorliegende Arbeit beschäftigt sich vor allem mit der Simulation des Ionenflusses in Nanoporen. Nanoporen könnten dank ihrer einfachen Ansatzes die Sequenzierung von DNA und die Analyse von Biomolekülen revolutionieren. In dieser Arbeit wird sowohl eine effiziente numerische Methode zur Lösung der partiellen Differentialgleichungen als auch eine Übersicht über die Simulationsergebnisse präsentiert. Dadurch soll ein besseres Verständnis der ablaufenden physikalischen Vorgänge ermöglicht werden.

Die Modellgleichungen sind durch ein zeitunabhängiges System partieller Differentialgleichungen gegeben, den stationären Poisson-Nernst-Planck-Stokes (oder Drift-Diffusions-Stokes-Poisson) Gleichungen. Die Wahl der Randbedingungen ist nicht trivial und wird explizit diskutiert.

Die numerische Methode zur Lösung dieser Gleichungen basiert auf der Methode der finiten Elemente und dem Newton-Verfahren. Die Methode wird weiters optimiert durch eine Adaptierung des verwendeten Gitters. Dadurch werden Rechenzeit und Aufwand niedrig gehalten, ohne Genauigkeit zu verlieren. Da Nanoporen oftmals rotationssymmetrisch aufgebaut sind, werden die Gleichungen auch für zylindrische Koordinaten formuliert und numerisch gelöst. Das freie Software-Paket FEniCS wurde zur Implementierung genützt, um den numerischen Lösungsprozess steuern und untersuchen zu können.

Die Simulationen werden für zwei Nanoporen, einer kleinen biologischen und einer größeren Solid-State Nanopore, genauer untersucht. An Hand von Strom-Spannungs-Kennlinien wird das Modell validiert. Gewisse Parameter müssen sorgfältig bestimmt werden, um Übereinstimmung zwischen Simulation und Experiment zu erhalten. Außerdem werden die Kräfte auf ein räumlich ausgedehntes Molekül für verschiedene Positionen simuliert. Die dadurch berechneten Kräfte werden unter anderem mit denen eines punktförmigen Moleküls verglichen. Ein Kraftfeld wird berechnet, um die Möglichkeit einer umfassenden Simulation von Nanoporen als Sensoren zu zeigen.

ACKNOWLEDGEMENTS

DANKSAGUNG

CONTENTS

LIST OF FIGURES

LIST OF TABLES

ACRONYMS

BC   Boundary condition

BD   Brownian dynamics

DDSP   Drift-diffusion-Stokes-Poisson

FEM   Finite element method

IC   Interface condition

ICR   Ion current rectification

IV   Current-voltage

MD   Molecular dynamics

NP   Nernst-Planck

PB   Poisson-Boltzmann

PDE   Partial differential equation

PNP   Poisson-Nernst-Planck

PNPS   Poisson-Nernst-Planck-Stokes

SAM   Self-assembled monolayer

INTRODUCTION

Nanopores excel at label-free single-molecule detection, including small molecules as well as charged polymers such as DNA and RNA. Thus, major applications of nanopores include DNA and RNA sequencing [41, 18, 11, 21, 7] and stochastic sensing of molecules [9, 70]. These applications can be summarized as nanopore analytics.

1.1 NANOPORE ANALYTICS

Nanopore analytics is based on modulations of ionic currents caused by molecules entering the nanoscale channel in the nanopore device. A molecule inside the channel briefly changes the electrical resistance of the nanopore system. A nanopore system typically consists of a nanopore, a tiny hole, inside a membrane, which divides two relatively large electrolyte reservoirs. The basic setup of a nanopore is shown in Figure 1. In each of the reservoirs an electrode is immersed
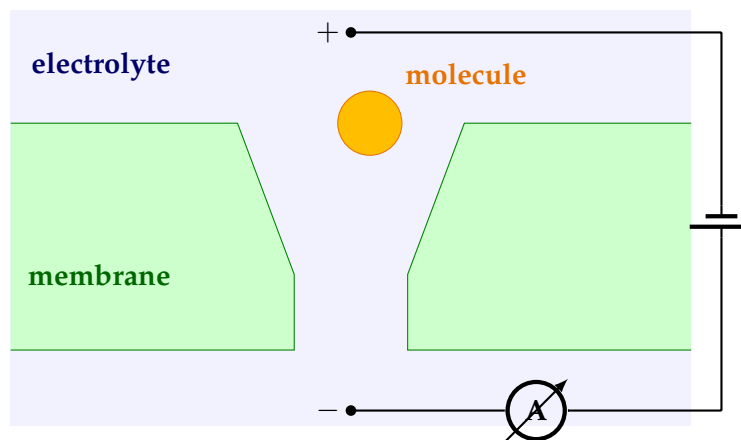
Figure 1: Basic setup, slightly modified from [58].

and a trans-membrane potential is applied, leading to an ionic current. The current is called *open pore current* if there is no particle inside the channel. Charged particles are pulled through the pore by the electrical field. If a particle enters the pore, it alters the ionic current due to its physical size and characteristics. Hence, particles can be detected by their associated current modulations. The princi-

ple is comparable to that of a Coulter counter. The simplicity of the approach makes nanopore analytics attractive.

Today there is a diverse field of man-made nanopores ranging from organic to inorganic materials [38]. The review articles [32, 38, 69, 57] give an accessible overview of the fast-growing research field. A relatively new type of nanopores are DNA origami nanopores, consisting of a self-assembled DNA spanning a lipid bilayer [14, 65, 46] or inserted into solid-state nanopores [11].

1.2 STATE-OF-THE-ART SIMULATIONS

The experimental research stimulates simulations of nanopores as sensors to provide a better quantitative understanding of the physics, which in turn can be enabled for rational design. There are several techniques for simulating nanopores, ranging from continuum models to Brownian dynamics (BD), also called stochastic dynamics, up to all-atom molecular dynamics (MD) models. The techniques differ largely in computational complexity, as in MD all atoms are treated explicitly, thus leading to high computational costs and limiting simulation time [55]. Also their scope of applications differs. MD simulations are well-suited for tiny nanopores, however, continuum models surpass them for bigger nanopores [23].

In this thesis the focus lies on a continuum model. State-of-the-art simulations relying on continuum models can be found in numerous papers. Most nanopore simulations with continuum models done so far use the commercial software COMSOL Multiphysics [71, 49, 26, 56, 54, 2, 47]. In contrast, simulations in this thesis are done with FEniCS, a free software package, which provides a flexible tool for the solution of partial differential equations (PDEs). Furthermore, it allows a thorough understanding and investigation of the numerical approach used in the solution process.

Different aspects of nanopore analytics have been analyzed, ranging from current simulations [72] to simulations of the effective driving force [54], which pushes the particle through the pore. Another interesting aspect for conical nanopores is ion current rectification (ICR) [66, 22], which leads to asymmetric current-voltage (IV) measurements. The effect of ICR is that IV curves are not symmetric anymore with regard to the applied voltage. This means that the current at negative voltages is different in magnitude than at positive voltages, in this case IV curves deviate from Ohmic behavior and become more diode like [2, 49, 71].

The targeted continuum model in this thesis consists of several PDEs, namely the Poisson-Nernst-Planck-Stokes (PNPS) equations. The PNPS equations are also called the drift-diffusion-Stokes-Poisson (DDSP) equations, see [34], where transport equations for nanopores are discussed. In short, the PNPS system essentially describes the electric field, the concentrations of the ions and the movement of the fluid under the applied electric potential. The PNPS equations are presented and solved numerically in 3D. One complication in the numerical solution process stems from the unstructured mesh due to the irregularities of realistic geometries. The irregularity of the mesh steered the numerical approach towards finite element method (FEM). Another complication is introduced by the instability of the Poisson-Nernst-Planck (PNP) system at relatively high charges or currents. This can be understood in terms of the local uniqueness of the PNP system.

In a bigger picture the ultimate goal is a comprehensible simulation of a stochastic single molecule sensor based on nanopore technology. This can be done by coupling the deterministic forces acting on the molecule with the indeterministic Langevin equation accounting for the Brownian motion of the molecule, similar to [40], but allowing off-centered particle paths. With these two ingredients plus a rate dependent simulation of the binding kinetics one obtains a mathematical description for a stochastic sensor. Thus, for a comprehensive sensor simulation a quantitative description of the flow and the forces acting on the molecule is necessary.

As the PNPS equations achieve equilibrium quickly, their characteristic time variable is smaller than the characteristic time variable of the Langevin equation. Thus, it is sufficient to solve the steady state PNPS equations for certain particle positions. For the slower stochastic motion of the particle the stationary solutions are then employed to solve the time dependent Langevin equation. In practice, the forces are only calculated for a specific set of particle positions in the fluid domain and are then interpolated on the whole fluid domain. The major benefit is that for a known configuration transient pore-molecule simulations are feasible within short computational time.

The focus of this thesis is to simulate the flow in nanopores. The thesis centers on the steady state part of the model described above. The steady state model includes a variety of interesting features, a selection of those is presented in this thesis. Since the numerical method chosen for the PDE system is an essential feature, it receives extra attention.

1.3   Overview of the Thesis

In Chapter 2, the assumptions on the model and the model equations are addressed. Boundary conditions for the continuum model are discussed in detail and an approximation of the model equations is introduced.

In Chapter 3, the numerical approach is presented. As the approach is based on FEM, the FEM method is shortly discussed. The actual solution process couples Newton's method and a fixed-point method to guarantee fast convergence. The convergence behavior and effectiveness of this approach is discussed.

In Chapter 4, simulations of realistic structures are presented. Two nanopores, one solid-state and one DNA origami pore, are discussed in detail. The focus lies on simulations of the current flow and on the computation of the driving forces.

Finally, conclusions are drawn in Chapter 5. In the appendix a list of physical constants and material parameters is provided.

MODEL

The goal in this chapter is a mathematical description of the movement of ions, water and large molecules inside a nanopore. Thus, the interest is in physical quantities such as the ionic currents and the effective force acting on a molecule, described in detail in Section 2.3. In order to be capable of calculating these quantities a description of the electrical field, the ionic concentrations and the flow of the solvent is necessary. The Poisson-Nernst-Planck-Stokes (PNPS) equations model the physics and are addressed in the upcoming Section 2.1. Later on boundary conditions (BCs) and interface conditions (ICs) for the PNPS system are specified in Section 2.2. An approximation of the electric field and the ionic concentrations is described in Section 2.4.

2.1 The Poisson-Nernst-Planck-Stokes (PNPS) System

The physical laws governing activity in a nanopore are modeled by a system of partial differential equations (PDEs). As outlined in the introduction, only a steady-state problem is examined. Hence some notes on the legitimacy of this approach will follow shortly. The problem can be seen as a multiscale problem in the following way. The translocation of a protein through the pore takes much longer than the time needed for the equilibrium of the PNPS system. This can be seen by looking at typical relaxation times of the different particles. Typical timescales for various processes are given in [59]. For example, water relaxes in around 10^{-14} s and ions in around 10^{-11} s. The typical timescale for the molecule relaxation is bigger than for ions, as molecules are larger. A molecule with radius bigger than 1 nm relaxes around an order of magnitude slower. Thus, the model for ions and water molecules is assumed to be time-independent.

As aforementioned, the system of PDEs should describe the electrostatics, the ion currents and the fluid flow. The model of choice consists of the Poisson, the Nernst-Planck (NP) and the Stokes equations; together they form the PNPS equations. In semiconductor physics, the NP equations are commonly referred to as the drift-diffusion

equations, thus another term for the PNPS system is drift-diffusion-Stokes-Poisson (DDSP) system [34].

Let us begin with the electrostatics, they are described by the well-understood Poisson equation

$$-\nabla \cdot (\epsilon \nabla \phi) = \rho_0 + e(c^+ - c^-) \, , \tag{2.1}$$

where ϵ is the permittivity, ϕ is the electrostatic potential, e is the (positive) elementary charge and ρ_0 is the permanent charge density, c^+ and c^- are the absolute concentrations of positive and negative ions, respectively. The permittivity ϵ can be written as $\epsilon = \epsilon_0 \epsilon_r$, where ϵ_0 is the vacuum permittivity and ϵ_r the relative permittivity of the material. The Poisson equation is solved on the whole domain Ω, which is the union of the fluid domain Ω_f and (possibly various) solid domains Ω_i.

The ion flow in the fluid domain Ω_f is described by the NP equations. Only the case for two ion species with valence ± 1 is considered, for example a solution of K$^+$ and Cl$^-$. The NP equations read

$$\nabla \cdot j^+ = 0 \, , \tag{2.2a}$$

$$\nabla \cdot j^- = 0 \, , \tag{2.2b}$$

$$j^+ = -e\left(D^+ \nabla c^+ + \mu^+ c^+ \nabla \phi - c^+ v\right) \, , \tag{2.2c}$$

$$j^- = e\left(D^- \nabla c^- - \mu^- c^- \nabla \phi - c^- v\right) \, . \tag{2.2d}$$

Here j^+ and j^- are the electric current densities of positive and negative ions, respectively, D^+ and D^- are the ion diffusion coefficients and μ^+ and μ^- are the electrical ion mobilities of positive and negative ions, respectively. The terms $c^+ v$ and $c^- v$ are nonstandard in the NP equations (2.2a)-(2.2d) and provide the link to the incompressible Navier-Stokes equations. The Navier-Stokes equations in conservative form on Ω_f read

$$-\nabla \cdot \left(\eta\left(\nabla v + \nabla v^{\mathrm{T}}\right) - \rho_{\text{fluid}}(v \otimes v) - p\mathbf{I}\right) = f_S \, ,$$
$$f_S = -e(c^+ - c^-)\nabla \phi \, , \tag{2.3}$$

$$\nabla \cdot v = 0 \, , \tag{2.4}$$

where v is the velocity field, ρ_{fluid} the fluid density, η the viscosity, p the pressure. The right hand side f_S of (2.3) represents the electric force on ions in the solvent. Equation (2.3) is derived from the principle of momentum conservation, whereas mass conservation infers the latter equation (2.4). Equation (2.4) is called the incompressibility equation in fluid mechanics. In order to justify an approximation of

the Navier-Stokes equation with the Stokes equations the Reynolds number Re has to be orders smaller than 1. The Reynolds number Re is defined by $Re := \frac{\rho_{\text{fluid}} v L}{\eta}$, where v is the characteristic velocity and L the characteristic length. The fact that $Re \approx 10^{-4} \ll 1$ justifies neglecting the quadratic velocity term in (2.3).

The conservative formulation or strain tensor formulation of the Stokes problem reads

$$
\begin{aligned}
-\nabla \cdot \sigma &= f_S \,, \\
\nabla \cdot v &= 0 \,,
\end{aligned}
\tag{2.5}
$$

with

$$
\sigma := -p\mathbf{I} + \eta(\nabla v + \nabla v^{\mathrm{T}}) = -p\mathbf{I} + 2\eta \operatorname{sym}(\nabla v)
\tag{2.6}
$$

denoting the stress tensor, where $\operatorname{sym}(\nabla v) := \frac{1}{2}(\nabla v + \nabla v^{\mathrm{T}})$ is the symmetric gradient.

By letting the incompressibility condition explicitly enter the momentum equation in the conservative Stokes system, the momentum equation can be written in the more common form

$$
\begin{aligned}
-\eta \Delta v + \nabla p &= f_S \,, \\
\nabla \cdot u &= 0 \,.
\end{aligned}
\tag{2.7}
$$

The Stokes system provides an adequate model of the viscous flow in the pore.

The PNPS system, (2.1)- (2.2d) and (2.5) or (2.7), is a coupled system of semilinear elliptic PDEs for the unknowns ϕ, c^+, c^-, v and p. A derivation of the PNPS model can be found in [64], which is inspired by [15]. In the former citation existence and uniqueness of solutions for a time-dependent PNPS problem are also analyzed.

The PNPS equations can be reformulated in terms of molar concentrations c^+ and c^- by slightly abusing notation and using the Faraday constant F

$$
\begin{aligned}
0 &= -\nabla \cdot (\epsilon \nabla \phi) - F(c^+ - c^-) - \rho_0 \,, &\tag{2.8a} \\
0 &= \nabla \cdot j^{\pm} \,, &\tag{2.8b} \\
j^{\pm} &= \mp F(D^{\pm} \nabla c^{\pm} \pm \mu^{\pm} c^{\pm} \nabla \phi - c^{\pm} v) \,, &\tag{2.8c} \\
0 &= -\eta \Delta v + \nabla p + F(c^+ - c^-) \nabla \phi \,, &\tag{2.8d} \\
0 &= \nabla \cdot v \,. &\tag{2.8e}
\end{aligned}
$$

The limitations of the Poisson-Nernst-Planck (PNP) model are discussed in Section 4.3. The relationship between diffusion coefficients

and electrical ion mobilities is given by the Einstein-Smoluchowski relation

$$\mu^{\pm} = \frac{eD^{\pm}}{k_B T} \; .$$

(2.9)

This relationship allows us to rewrite the current densities in the following form

$$j^{\pm} = \mp F\left(D^{\pm}(\nabla c^{\pm} \pm \frac{e}{k_B T}c^{\pm}\nabla\phi) - c^{\pm}v\right) \; .$$

(2.10)

Furthermore, the ion mobility in the pore is lower according to [36] due to the confined structure. This means that the diffusion constant D is modeled by different constants in and outside the pore. This issue is going to be discussed in Chapter 4.

2.2   BOUNDARY AND INTERFACE CONDITIONS

In this section the BCs of the PDE system are specified. Furthermore, to include permanent charges sitting on the interfaces of charged solid parts and the fluid ICs are employed. Hence, the permanent charges of the membrane and the DNA are included via surface charges at the interfaces. The surface charge ρ_S is assumed to be constant along the interface with a value according to the adjacent materials, e. g. ρ_{DNA} for the DNA boundary. The interfaces are denoted by $\Gamma_i = \overline{\Omega_f} \cap \overline{\Omega_i}$, where i is some solid domain, e. g. SiN.

For the Poisson equation the *interface condition*

$$\left[\epsilon\nabla\phi \cdot n\right]_{\Gamma_i} = \rho_S\big|_{\Gamma_i}$$

(2.11)

holds. Here $[\psi]_\Gamma = \psi(+) - \psi(-)$ denotes the jump operator, which is unequal to zero for discontinuous functions ψ at Γ. The charge of the molecule Q_M is smeared over the whole volume V_M of the ball, i. e. $\rho_S\big|_{\Gamma_M} = 0$ and $\rho_0 = Q_M/V_M$. Even if there is no surface charge present, the interface conditions result in a discontinuous electric field $-\nabla\phi$ across the interfaces for different permittivities.

Coming back to the BCs, the applied potential of the electrodes is included via Dirichlet boundary conditions on the top and bottom boundary. To make the computational effort smaller, the computational domain is truncated to the vicinity of the pore. That it is reasonable to still apply the biased voltage in a vicinity of the pore is outlined in the following paragraph.

In order to keep the approach simple, the solvent is modeled by a series of resistors. This means that for an applied electrode potential

U the transmembrane potential near the pore can be calculated by treating the whole system as a series circuit. In a series circuit, the current is the same at each point in the circuit, thus by Ohm's law

$$U = R_{total} I = 2R_f I + R_p I \,, \tag{2.12}$$

where R_f is the resistance of the solvent above and below the pore and R_p is the resistance of the solvent in the pore. The resistance R of an electrolyte is given by

$$R = \frac{l}{\kappa S} \,,$$

where l is the length of the considered domain, S the area of its cross-section and κ the local electrolyte conductivity. The conductivity κ of the solvent is known and given by [54]

$$\kappa = F(\mu^+ c^+ + \mu^- c^-) \,. \tag{2.13}$$

The pore resistance R_p for a conical pore can be approximated by

$$R_p = \frac{4}{\pi \kappa} \frac{l_p}{d_p D_p} \,, \tag{2.14}$$

where l_p, d_p and D_p are the pore's length and the diameter of the pore at the narrow tip and at the larger base, respectively. This approximation is a very simple geometric mean approximation, also used in [6] for a conical pore. For the fluid resistance R_f, a cylindrical electrolyte reservoir of length $l_f = 1 \mu m$ and diameter $d_f = D_f = 1 \mu m$ is considered. Then, if $l_p \approx 10$ nm and $D_P \approx 10$ nm $\approx d_p$, it holds that

$$\frac{l_p}{d_p D_p} = 10^8 \gg 10^6 = \frac{l_f}{d_f D_f} \,.$$

Thus, the potential drop of the solvent outside the pore is neglected and the applied potential U is prescribed as a transmembrane potential $\Delta V = U$ in the vicinity of the pore. Moreover, the presented estimation neglects dielectric double layers near charged boundaries, especially the electrical double layer near the electrodes. Dirichlet BCs for the potential on the top and bottom boundary of the computational domain were used. In the simulations, the top boundary is grounded and at the bottom of the computational domain the potential drop ΔV is set as an inhomogeneous Dirichlet BC. At the side boundaries insulating BCs are specified, assuming that these boundaries are far enough away and hence are not influencing the electrical potential near the pore.

For the NP equations, homogeneous Neumann BCs

$$j \cdot n = 0,$$

are imposed on the interfaces Γ_i, where n is the outward normal of the fluid domain. This corresponds to the requirement that there should be no ionic flow through the fluid-solid interfaces. At the top and bottom fluid boundaries of the computational domain inhomogeneous Dirichlet BCs are applied to keep the concentration at the reservoir at bulk value.

The BCs for the Stokes equations are a mix of no-slip and stress-free BCs. On the surfaces of the solid no-slip BCs given by $v = 0$ are prescribed. The no-slip BCs can be seen as homogeneous Dirichlet boundary conditions for the velocity v. On the top, side and bottom boundaries no-stress or stress-free BCs are chosen. As remarked in Section 12.1.4 in [48], the appropriate choice for modeling flow into a large reservoir are stress-free BCs $\sigma \cdot n = 0$. These BCs are vanishing in the case of the strain tensor formulation of the Stokes problem. So they can be seen as "do-nothing" BCs for the conservative formulation. The term "do-nothing" refers to artificial boundary conditions that are implicitly given in the variational forms [35]. They differ from the natural flow condition $(\nabla v - p\mathbf{I}) \cdot n = 0$. For the non-conservative form of the Stokes problem (2.7), the natural outflow conditions are analogous to Neumann BCs for the Poisson problem. The natural flow BCs are also referred to as the "do-nothing" BCs because with these BCs, the Neumann boundary term vanishes in the non-conservative weak formulation of the Stokes problem.

2.3 Physical Quantities of Interest

As mentioned in the beginning of this chapter, the goal is to compute the effective force acting on a molecule and the pore current. The effective force F_{eff} is composed of a bare electric force F_{el} and a drag force F_{drag}:

$$F_{\text{eff}} = F_{\text{el}} + F_{\text{drag}} . \tag{2.15}$$

The electric force originates from the action of the electric field on the charged molecule. The electric field is induced by the electrodes and the charged surface inside the pore. It is given by

$$F_{\text{el}} = -\int_M \rho_M \nabla \phi \, dx . \tag{2.16}$$

Molecule charges are not modeled as discrete point charges. Instead, they are smeared out across the whole molecule resulting in a volume charge density ρ_M.

The drag force sums up the interactions of the solvent particles with the molecule and is given by

$$F_{\text{drag}} = \int_{\partial M} n \cdot \left(- \eta \left(\nabla v + \nabla v^{\text{T}} \right) + p\mathbf{I} \right) ds . \tag{2.17}$$

The drag force can also be expressed as the sum of the viscous stress force

$$F_{\text{shear}} = -2 \int_{\partial M} n \cdot \eta \, \text{sym}(\nabla v) \, ds \tag{2.18}$$

and the pressure stress force

$$F_{\text{P}} = \int_{\partial M} n \cdot p\mathbf{I} \, ds . \tag{2.19}$$

The current I is given by surface integrals over a cross-section C of the nanopore and is positively oriented along the z-direction

$$I = \int_C \left(j_z^+ + j_z^- \right) \, ds . \tag{2.20}$$

2.4 THE POISSON-BOLTZMANN (PB) EQUATION

The Poisson-Boltzmann (PB) equation is an often-used approximation for the PNP equations in the solvent. In this section no hydrodynamic coupling is assumed, i.e. $v = 0$ in the PNP equations. The PB equation is capable of providing a good estimate for the ion concentrations in electrical double layers at equilibrium and at low voltages. The linear PB equation is also called Debye-Hückel approximation due to their classic paper [24].

In the PB approximation, the ion concentrations are assumed to satisfy equilibrated Boltzmann distributions

$$c^{\pm} = c_0 \exp\left(\mp \frac{e\phi}{k_B T} \right) , \tag{2.21}$$

with a potential ϕ. The zero in potential corresponds to the bulk concentration c_0, essentially ϕ equals zero far away from any charged object. Plugging (2.21) into (2.8a) yields the nonlinear PB equation

$$-\nabla \cdot (\epsilon \nabla \phi) = -2Fc_0 \sinh\left(\frac{e\phi}{k_B T} \right) ,$$

where permanent charges are omitted for simplicity of presentation. Another often-used simplification is the linearization of the ion concentration in the Boltzmann distribution (2.21) by assuming $\frac{e\phi}{k_B T} \ll 1$. Then

$$c^{\pm} = c_0 \exp\left(\mp \frac{e\phi}{k_B T} \right) \approx c_0 \left(1 \mp \frac{e\phi}{k_B T} \right) . \tag{2.22}$$

Using this linear approximation in (2.8a) yields the linearized PB equation,

$$-\nabla \cdot (\epsilon \nabla \phi) = F(c^+ - c^-) = -2Fc_0 \frac{e\phi}{k_B T} \; . \tag{2.23}$$

For constant permittivity this can be simplified to

$$\nabla \cdot (\nabla \phi) = \frac{\phi}{\lambda_D^2} \; .$$

where

$$\lambda_D = \sqrt{\frac{\epsilon k_B T}{2eFc_0}}$$

is the so-called Debye length. The PB approximation can also be viewed in the following way. Instead of prescribing flux conservation in (2.8b), vanishing fluxes are prescribed everywhere, i.e. $j^\pm = 0$ in (2.10). If permanent charges are included, the linear PB equation reads

$$-\nabla \cdot (\epsilon \nabla \phi) = -2Fc_0 \frac{e\phi}{k_B T} + \rho_0 \; , \tag{2.24}$$

with appropriate boundary and interface conditions.

The PB approximation is actually not a direct part of the model. But it is used later for mesh prerefinement, cf. Section 3.6.2, as the PB equation provide a computationally cheap approximation to the PNP system.

METHODS

In order to solve the system of partial differential equations (PDEs) the finite element method (FEM) was employed. One of the major advantages of FEM is that it can handle irregularities in realistic geometries. The problem of resolving a complicated geometry is passed down to mesh generators. There exist FEM packages which enable an easy and simple implementation, e. g. FEniCS [50].

The Poisson-Nernst-Planck-Stokes (PNPS) system was solved iteratively by a hybrid approach. This means that the numerical solution was computed by using a fixed-point iteration consisting of solving alternatively a Newton step of the Poisson-Nernst-Planck (PNP) system and a subsequent iteration of the Stokes system. This proved beneficial since it is computationally cheaper and faster than a Newton iteration of the full PNPS system. Moreover, the separation splits the coupled PNPS equations into two systems which are relatively well understood.

In this chapter, FEM is briefly reviewed in Section 3.1. Weak formulations of the PNP and Stokes equations are stated and the hybrid Newton-Picard iteration is described in more detail from Section 3.2 to Section 3.4. Also, the numerics of the PNP and Stokes equations are investigated in these sections. In Section 3.5, an axisymmetric formulation in cylindrical coordinates is provided. Furthermore, some notes on adaptivity, the computation of the goal quantities and iterative solvers are given in Section 3.6, Section 3.7 and Section 3.8, respectively. Implementation and mesh generation are discussed in Section 3.9.

3.1 The Finite Element Method

In this section only a short introduction to the FEM is provided, as this method is quite popular and well-covered by a large amount of textbooks. For an accessible introduction to FEM, which also covers implementational aspects [31] can be recommended. For a more rigorous mathematical treatment see [13] or [48]. First, let us state the abstract mathematical framework.

3.1.1   Abstract Framework

In the following, a basic knowledge of Sobolev spaces and their properties is assumed. For a comprehensive textbook on Sobolev spaces and their properties see [1]. Also most books about abstract FE analysis, e. g. [13], dedicate a chapter to Sobolev spaces.

Let $(V, (\cdot, \cdot)_V)$ be a Hilbert space with inner product, for example $H_0^1(\Omega)$, the Sobolev space with differentiability index 1 and homogeneous boundary conditions (BCs). Furthermore, let $a : V \times V \to \mathbb{R}$ be a bilinear form that is

(a) *coercive*: $\exists\, \alpha > 0 : \ a(v, v) \geq \alpha \|v\|_V^2$, and

(b) *continuous*: $\exists\, C_a > 0 : \ a(u, v) \leq C_a \|u\|_V \|v\|_V$,

and $l : V \to \mathbb{R}$ be a continuous ($\exists\, C_l > 0 : \ l(v) \leq C_l \|v\|_V$) linear functional. Consider the following variational problem: find $u \in V$ such that

$$a(u, v) = l(v) \qquad \forall v \in V . \tag{3.1}$$

In view of showing existence and uniqueness for this variational problem the following theorems are well-known.

THEOREM 3.1 (Riesz representation theorem). *Let $(V, (\cdot, \cdot))$ be a Hilbert space with inner product. Every continuous linear form $l(\cdot)$ on V can be uniquely represented as*

$$l(v) = (u, v)$$

for some $u \in V$.

so, if the bilinear form a is symmetric, it defines an inner product and therefore the existence and uniqueness of a solution of (3.1) directly follows from the Riesz representation theorem. More interesting is the non-symmetric case.

THEOREM 3.2 (Lax-Milgram Lemma). *Let $(V, (\cdot, \cdot))$ be a Hilbert space with inner product. Let $a(\cdot, \cdot)$ be a coercive continuous bilinear form on V, and let $l(\cdot)$ be a continuous linear form on V. Then there exists a unique solution $u \in V$ to the abstract variational problem (3.1).*

For the theorems and the proofs see for example Section 7.3 in [48].

3.1.2   The Galerkin Method

The starting point for every discretization is a variational formulation of the corresponding PDE. The goal is to approximate the solution u in the possibly infinite-dimensional Hilbert space V of the problem: find $u \in V$ such that

$$R(u,v) := a(u,v) - l(v) = 0 \qquad \forall v \in V , \tag{3.2}$$

where R denotes the residual of the variational problem. In the Galerkin method, one chooses finite-dimensional trial and test function spaces W_h and V_h, respectively. If the trial and test function space coincide, then the method is referred to as *Bubnov-Galerkin* method. If the space V_h is a subset of V one speaks of *conforming FEM*. The Galerkin formulation of the variational problem (3.2) reads: find $u_h \in V_h \subseteq V$, the so-called *Galerkin projection* of u, such that

$$R(u_h, v_h) = 0 \qquad \forall v_h \in V_h \subseteq V. \tag{3.3}$$

The existence and uniqueness of the discrete variational problem is inherited from the continuous case. Subtracting (3.3) from (3.2) yields the important Galerkin orthogonality

$$a(u - u_h, v_h) = R(u - u_h, v_h) = 0 \qquad \forall v_h \in V_h \subseteq V .$$

Another important result is Céa's lemma, also known as quasioptimality or best approximation result:

$$\|u - u_h\|_V \leq \frac{C_a}{\alpha} \|u - v_h\|_V \qquad \forall v_h \in V_h ,$$

where C_a and α are the continuity constant and coercivity constant of a, respectively. Céa's lemma is inferred from Galerkin orthogonality and establishes the fact that up to a constant the approximation u_h is as best as it can be in V_h. By choosing a specific v_h, usually an interpolation of u, one can derive an a priori error estimate for the error $u - u_h$ in V with the help of interpolation estimates.

3.1.3   The Finite Element Method

The finite element method (FEM) is Galerkin's method with finite dimensional subspaces V_h consisting of piecewise polynomial functions. The subdomains K on which the polynomials are defined are called elements of the mesh or tessellation $\mathcal{T}$ on Ω. Details for the formal definition of FEM can be found, e.g. in Chapter 3 of [13]. Later on some notation for FEM subspaces is needed, thus let

$$S^p(\mathcal{T}) := \left\{ \psi_h \in C^0(\Omega) \middle| \; \psi_h|_K \text{ is a polynomial of degree } p \right\} \tag{3.4}$$

3.1.4   Application to the Linear PB Problem

The standard Galerkin method is demonstrated on the linear Poisson-Boltzmann (PB) problem (2.23) as an application of the abstract framework derived in the subsection above.

First, a weak formulation of the PB problem is derived. The advantage of a weak formulation is that requirements on the regularity of the solution u can be dropped, in contrast to the strong formulation. The starting point is the original PDE or so-called strong form of the linear PB equation (2.24) for the potential ϕ. The assumption that no potential is applied corresponds to homogeneous Dirichlet BCs. As Dirichlet BCs are included in the function space, the Hilbert space $V = \{v \in H^1(\Omega) : v|\partial\Omega = 0\}$ with norm $\|v\|_V = \|v\|_{H^1}$ is well-suited for our needs. In the case of homogeneous Dirichlet BCs, Friedrichs' inequality shows that the H^1-norm is equivalent to $\|\nabla v\|_{L^2}$ for all $v \in V$.

Furthermore, a partition of the domain Ω into finitely many subdomains Ω_i on which the permittivity ϵ and the bulk concentration c_0 are constant is assumed. On the interface Γ_i the interface condition (2.11) is prescribed. To be precise, positive permittivities and zero bulk concentration are assumed everywhere, except on the fluid subdomain Ω_f. There, a positive bulk concentration is assumed.

The weak formulation is derived by multiplying original PDE (2.23)

$$-\nabla \cdot (\epsilon \nabla \phi) = -2Fc_0 \frac{e\phi}{k_B T}$$

with some test function $\psi \in V$ and by integrating on each subdomain. Then a subsequent integration by parts and substitution of the interface conditions (ICs) yields

$$\sum_i \left(\int_{\Omega_i} \epsilon_i \nabla \phi \cdot \nabla \psi \, dx + \int_{\Omega_i} kc_0 \phi \psi \, dx - \int_{\Gamma_i} \rho_S \psi \, ds \right) = 0 \,,$$

where $k = 2Fe/k_B T > 0$. By defining the bilinear form a_{PB} and the linear form l_{PB} the following variational problem has to be solved: find ϕ in V such that

$$a_{\text{PB}}(\phi, \psi) := \int_\Omega \epsilon \nabla \phi \cdot \nabla \psi \, dx + \int_{\Omega_f} kc_0 \phi \psi \, dx$$

$$= \int \rho_S \psi \, dx =: l_{\text{PB}}(\psi) \, dx \qquad \forall \psi \in V.$$

Both the bilinear form $a_{\text{PB}} : V \times V \to \mathbb{R}$ and the linear form $l_{\text{PB}} : V \to \mathbb{R}$ are continuous. That the bilinear form a_{PB} is continuous

is straightforward. The continuity of l_{PB} can be seen by the trace inequality. Coercivity of a_{PB} follows from

$$a_{\mathrm{PB}}(u,u) \geq \min_i \epsilon_i \|\nabla u\|^2_{L^2(\Omega)} + kc_0 \|u\|^2_{L^2(\Omega_f)} \geq \min_i \epsilon_i \|\nabla u\|^2_{L^2(\Omega)}$$

and the equivalence of the norms $\|\cdot\|_V$ and $\|\nabla(\cdot)\|_{L^2(\Omega)}$. The variational Poisson problem can be restated in the abstract framework: find $u \in V$ such that

$$a_{PB}(u,v) = l_{PB}(v) \qquad \forall v \in V. \tag{3.5}$$

Now existence and uniqueness of the solution of the above problem (3.5) is guaranteed by the Lax-Milgram Lemma.

It is also possible to use FEM for the nonlinear elliptic PB equation. An analysis of the PB equation with additional point charges can be found in [17]. In [37] an adaptive FEM is developed for the nonlinear PB system and a priori estimates are given.

3.2 HYBRID APPROACH FOR THE PNPS SYSTEM

One goal of this thesis was the implementation of an efficient numerical solver, especially in terms of goal functionals like the current or the effective driving force applied on proteins. In pursuance of this goal, the following two features proved important for a successful numerical method:

1. a well-adapted mesh (regarding the target quantities),

2. an efficient solver for the PNPS system.

Obviously both steps should be done in an economical manner, considering computational time and memory consumption.

To tackle the first issue, the initial mesh from the mesh generator was refined with a goal adaptive refinement strategy; this is described in detail in 3.6.2. For the second part a hybrid approach proved beneficial. As the standard way to solve the PNP equations is Newton's method [53], the proposed hybrid algorithm is:

While updates are bigger than a tolerance tol repeat the following steps:

1. Solve a Newton step for the PNP equations.

2. Solve the Stokes system.

That means that for each solution of the Newton step, the Stokes equations are solved and then the velocity is plugged back into the

Newton step of the PNP equations. In view of this decoupling, the Stokes system becomes linear. Only the right hand side changes at each iteration, so the stiffness matrix of the Stokes problem can be reused for all hybrid iterations. This is reasonable because numerical evidence showed that the Nernst-Planck (NP) equations and the Stokes equation are weakly coupled, meaning that the terms linking the Stokes and the NP equations are relatively small. This can also be seen by the relatively small currents coming from the Stokes term pointing in the axis direction, cf. Section 4.6.2. Essentially, the hybrid approach means that the nonlinear coupling of the Stokes and the NP equations is treated iteratively instead of a comprehensive Newton step.

The decoupling of the PNPS system has the advantage that the solution process is cheaper and faster. Since Newton's method converges quadratically it is not a priori clear if Newton's method including Stokes' equation, from now on referred to as *full Newton's method*, or the hybrid approach is faster. However, the computational time is worse for the full Newton's method compared to the hybrid approach, even though it needs fewer iterations. This is shown by Figure 2B and Figure 2A, respectively. In terms of memory consumption the hybrid approach needs around half the memory resources compared to the full Newton system in the axisymmetric case.

One might ask: Why not also decouple the PNP system? Numerical experiments showed that a Picard iteration of alternatively the Poisson equation and the NP equations diverged for moderately large potentials or surface charges. In this context this means not as large as in experiments and not so large that Newton's method is unstable (as for large potentials).

3.3   The Poisson-Nernst-Planck (PNP) System

As already noted, the proposed way to solve the PNP equations is a (possibly damped) Newton's method. Thus, Newton-like methods for Galerkin FEM are briefly discussed.

3.3.1   Newton-like Methods

In this section, a Newton-like method for FEM with a nonlinear weak form $\langle F(x), y \rangle = 0$, where $F : H \to H^*$, H^* denoting the topological
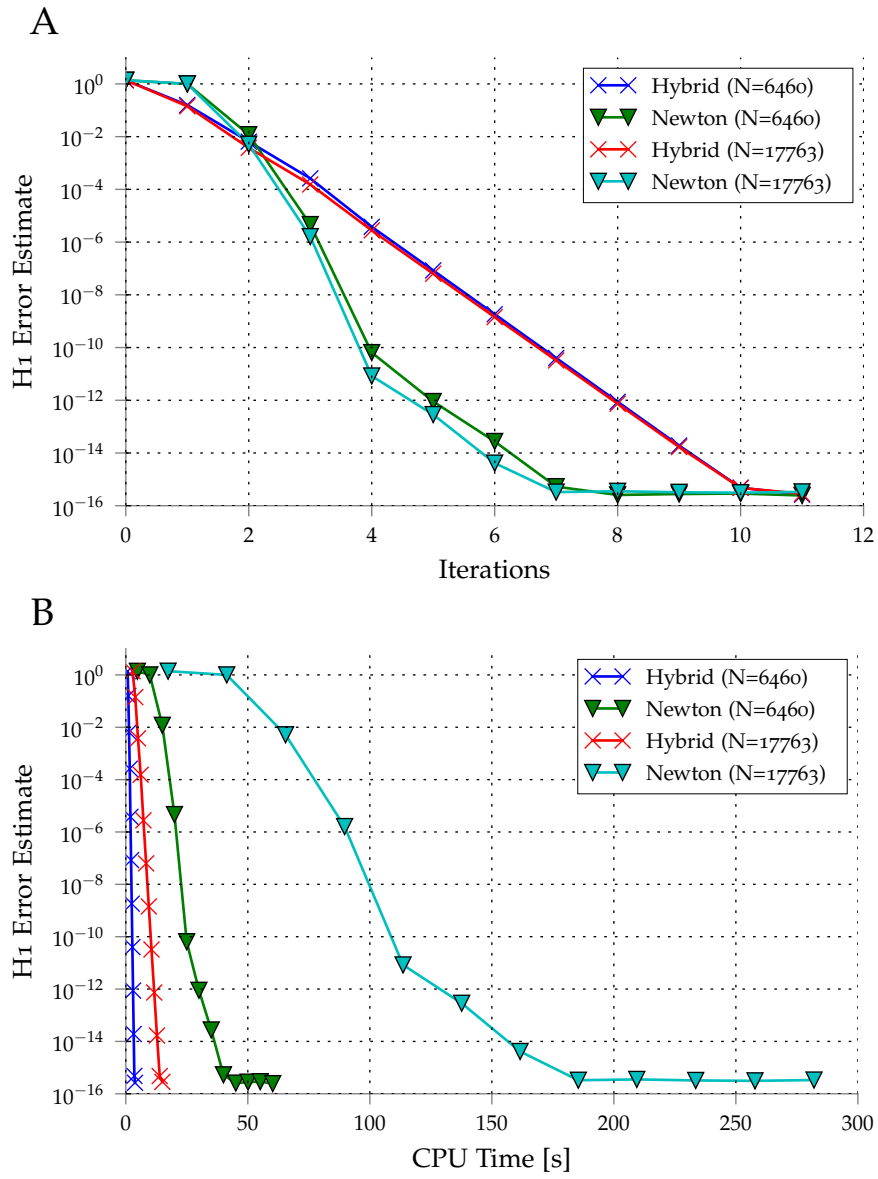
Figure 2: Comparison of hybrid and Newton method for two meshes
        with a different number of elements N.
        A. Comparison in terms of error over iterations.
        B. Comparison in terms of error over CPU time.

dual of a Hilbert space H and duality pairing $\langle \cdot, \cdot \rangle$, is motivated. The Gâteaux-derivative $\mathbf{D}F(x)$ at $x \in H$ is defined by the bilinear form

$$\langle \mathbf{D}F(x)z, y \rangle = \frac{d}{d\tau} \langle F(x + \tau z), y \rangle \Big|_{\tau=0} , \qquad (3.6)$$

where $z, y \in H$. Taking x as the sum of an approximation $\hat{x}$ plus some correction δx, i.e. $x = \hat{x} + \delta x$, then linearizing F around $\hat{x}$ yields

$$0 = \langle F(x), y \rangle = \langle F(\hat{x} + \delta x), y \rangle = \langle F(\hat{x}), y \rangle + \langle \mathbf{D}F(\hat{x}) \delta x, y \rangle .$$

This observation motivates the following algorithm:

- Choose an initial guess x_0, a tolerance tol and a damping parameter λ.

- While $\|\delta x\| \geq$ tol :
    1. Solve $\langle \mathbf{D}F(\hat{x}) \delta x, y \rangle = -\langle F(\hat{x}), y \rangle$ for δx.
    2. Update $\hat{x}$ with $\hat{x} + \lambda \, \delta x$.

3.3.2   Newton Method for the PNP System

In the concrete case of the PNP equations the nonlinear weak form is defined by

$$\langle F(x), y \rangle = \begin{pmatrix} (\epsilon \nabla \phi, \nabla \psi) - F(c^+ - c^-, \psi) - (\rho_0, \psi) - (\rho_S, \psi)_{\Gamma_i} \\ (D^+ \nabla c^+, \nabla \vartheta^+) + (\mu^+ c^+ \nabla \phi, \nabla \vartheta^+) - (c^+ v, \nabla \vartheta^+) \\ (D^- \nabla c^-, \nabla \vartheta^-) - (\mu^- c^- \nabla \phi, \nabla \vartheta^-) - (c^- v, \nabla \vartheta^-) \end{pmatrix} ,$$

where $x = (\phi, c^+, c^-)$ in $H = H^1(\Omega) \times H^1(\Omega_f) \times H^1(\Omega_f)$ with appropriate BCs and $y = (\psi, \vartheta^+, \vartheta^-)$ in H. Here also the Stokes term is included, where v is considered as a given function. Thus, the Gâteaux derivative $\mathbf{D}F(x)$, cf. (3.6), of F in direction of $z = (\varphi, \theta^+, \theta^-)$ reads

$$\langle \mathbf{D}F(x)z, y \rangle = \begin{pmatrix} (\epsilon \nabla \varphi, \nabla \psi) - F(\theta^+ - \theta^-, \psi) - (\rho_0, \psi) - (\rho_S, \psi)_{\Gamma_i} \\ (D^+ \nabla \theta^+, \nabla \vartheta^+) + \mu^+ (\theta^+ \nabla \phi + c^+ \nabla \varphi, \nabla \vartheta^+) - (\theta^+ v, \nabla \vartheta^+) \\ (D^- \nabla \theta^-, \nabla \vartheta^-) - \mu^- (\theta^- \nabla \phi + c^- \nabla \varphi, \nabla \vartheta^-) - (\theta^- v, \nabla \vartheta^-) \end{pmatrix} .$$
$$(3.7)$$

3.3.3   Discretization of the PNP System

For the discretization, the finite dimensional subspace $S^1(\mathcal{T})$ with homogeneous BCs was used for each component of H. The inhomogeneous Dirichlet BCs of the PNP equations are applied to the initial guess x_0. This is slightly different from the usual FEM setting, where the Dirichlet BCs enter the trial function space.

3.4   STOKES SYSTEM

This section is largely based on Chapter 12 in [48]. Saddle-point problems, of which the Stokes problem is a special case, are discussed. For saddle-point problems the choice of FE spaces is a delicate matter, so a closer look is taken in Section 3.4.3. For simplicity of presentation in this section $\eta = 1$ is assumed. Furthermore, the analysis is restricted to the non-conservative form of the Stokes problem with homogeneous Dirichlet BCs.

3.4.1   Weak Formulation

Let U, Q be Hilbert spaces and define the forms

$$a_S(u,v) := (\nabla u, \nabla v) , \tag{3.8}$$
$$b_S(u,q) := -(\nabla \cdot u, q) , \tag{3.9}$$
$$l_S(v) := (f,v) .$$

Then a weak formulation of the Stokes problem reads: find $(u,p) \in U \times Q$ such that

$$a_S(u,v) + b_S(v,p) = l_S(v) \qquad \forall v \in V , \\ b_S(u,q) = 0 \qquad \forall q \in Q . \tag{3.10}$$

Sometimes the sign of the pressure p is flipped or the second equation in (3.10) is multiplied by -1, to yield a system that is positive definite, but no longer symmetric. As already noted, the Stokes system (3.10) has the structure of a saddle-point problem, which is quite different from that of the Poisson equation. It will turn out that things are more difficult in this case. By defining a bilinear form

$$B((u,p),(v,q)) := a_S(u,v) + b_S(v,p) + b_S(u,q) \tag{3.11}$$

and a linear form $F((v,q)) = l(v)$ another weak formulation can be derived: find $(u,p) \in U \times Q$ such that

$$B((u,p),(v,q)) = F((v,q)) \qquad \forall (v,q) \in U \times Q . \tag{3.12}$$

3.4.2   Inf-Sup Condition

Existence and uniqueness of the Stokes problem are shortly discussed. The goal here is to derive some kind of coercivity on the bilinear form B in (3.11). As $b_S(u,p) = 0$, it follows that

$$B((u,p),(u,p)) = a_S(u,u) .$$

This shows that there is no hope of showing coercivity in the usual way, as the norm of the pressure is missing in the coercivity inequality $B((u,p),(u,p)) \geq \alpha(\|u\|^2 + \|p\|^2)$. Thus, one has to establish a different condition or one can modify the bilinear form to acquire coercivity. The latter possibility of modifying the bilinear form such that it is coercive on $U \times Q$ is discussed in Section 3.4.5. In order to show well-posedness for (3.10) define the closed null space $Z = \{v \in U : b(v,q) = 0 \ \forall q \in Q\} \subset U$, which incorporates the incompressibility condition. Then the following problem needs to be solved: find $u \in Z$ such that

$$a_S(u,v) = l_S(v) \qquad \forall v \in Z .$$

That this problem is well-posed can be deduced from Lax-Milgram, because a_S is coercive. It remains to show that the pressure problem: find $p \in P$ such that

$$b_S(v,p) = l_S(v) - a_S(u,v) \qquad \forall v \in U ,$$

is also well-posed. The existence and uniqueness of this problem is implied by the following theorem, known as Ladyshenzkaya-Babuška-Brezzi theorem.

THEOREM 3.3 (LBB). *Let U, Q be Hilbert spaces and $a(\cdot,\cdot) : U \times U \to \mathbb{R}$ and $b(\cdot,\cdot) : U \times Q \to \mathbb{R}$ be continuous bilinear forms. If additionally b_S fulfills the inf-sup condition: There exists $\beta > 0$ such that*

$$\inf_{q \in Q \setminus \{0\}} \sup_{v \in V \setminus \{0\}} \frac{b(v,q)}{\|v\|_V \|q\|_Q} \geq \beta . \qquad (3.13)$$

Then the problem

$$b_S(v,p) = \tilde{F}(v) := l_S(v) - a_S(u,v) \qquad \forall v \in U$$

has a unique solution.

See Lemma 10.2.12 in [13] for a proof. In view of this theorem it follows that the Stokes problem (3.10) has a unique solution if a_S is continuous and coercive and if b_S is continuous and fulfills the inf-sup condition. The only requirement that is not easy to show is the inf-sup condition for b_S. That the inf-sup condition holds follows from the following theorem (see Section 12.2.4 in [48])

THEOREM 3.4 (Inf-Sup Condition). *Let $U = H_0^1(\Omega)^d$ and $Q = L_0^2(\Omega)$, where $L_0^2(\Omega) := \{q \in L^2(\Omega)| \int_\Omega q = 0\}$. Then b_S defined as in (3.9) satisfies the inf-sup condition (3.13).*

3.4.3   Discretization of the Stokes System

After having shown existence and uniqueness in the continuous case, the next step is the discrete case. Choosing finite-dimensional subspaces U_h and Q_h the discrete FEM problem reads: find $(u_h, p_h) \in U_h \times Q_h$ such that

$$
\begin{aligned}
a_S(u_h, v_h) + b_S(v_h, p_h) &= l_S(v_h) \quad \forall v_h \in V, \\
b_S(u_h, q_h) &= 0 \qquad \forall q_h \in Q_h .
\end{aligned}
\tag{3.14}
$$

In order to establish discrete well-posedness similar to the continuous case a discrete inf-sup condition on the discrete spaces U_h and Q_h has to be shown

$$
\inf_{q \in Q_h \setminus \{0\}} \sup_{v \in V_h \setminus \{0\}} \frac{b_S(v, q)}{\|v\|_{V_h} \|q\|_{Q_h}} \geq \beta .
\tag{3.15}
$$

However, even conforming spaces $U_h \subset U$ and $Q_h \subset Q$ may violate the discrete inf-sup condition (3.15), despite of holding in the continuous case. One technique to somehow transfer the continuous inf-sup condition to the discrete case is Fortin's trick, which will not be described in detail.

A method often-used for constructing spaces that satisfy the discrete inf-sup condition is the following. Keep the degrees of freedom for the pressure space fixed, while making the space for the velocity rich enough. This can be motivated by

$$
\inf_{q \in Q_h \setminus \{0\}} \sup_{v \in V \setminus \{0\}} \frac{b_S(v, q)}{\|v\|_V \|q\|_Q} \geq \inf_{q \in Q \setminus \{0\}} \sup_{v \in V \setminus \{0\}} \frac{b_S(v, q)}{\|v\|_V \|q\|_Q} \geq \beta .
$$

To this end a higher polynomial degree for the velocity test functions or a macroelement technique can be used. The macroelement technique focuses on subdomains, so-called *macroelements*, on which the inf-sup condition is established. Then these stable macroelements are patched together. Details for these methods can be found in Chapter 3 in [27].

Additionally for the mixed case, a quasioptimality result can be shown under certain assumptions, see Cor. 10.5.18 in [13].

THEOREM 3.5. *Let (u, p) denote the solution to the problem (3.10) and let (u_h, p_h) denote the solution to the discrete problem (3.14). There is a constant c depending on the continuity constant C of a and l, the coercivity constant α of a and the discrete inf-sup constant β_h such that*

$$
\|u - u_h\|_V + \|p - p_h\|_Q \leq c \left(\inf_{v \in V_h} \|u - v\|_V + \inf_{q \in Q_h} \|p - q\|_Q \right). \tag{3.16}
$$

The choice $U_h = S^1(\mathcal{T})^d$ and $Q_h = S^0(\mathcal{T}) \cap L_0^2(\Omega)$ would be nice for $U = H^1(\Omega)^d$ and $Q = L_0^2(\Omega)$ since this would yield the same order on both errors. But this choice for U_h and Q_h unfortunately violates the discrete inf-sup condition.

Two discretization methods that fulfill the discrete inf-sup condition are presented, the Taylor-Hood discretization and an equal-order stabilized system. The Stokes system with the lowest-order Taylor-Hood discretization consumes a lot of memory, therefore it is expensive. To remedy these shortcomings in the simulations the stabilized equal order piecewise linear discretization was employed.

3.4.4   Taylor-Hood

The *Taylor-Hood* approximation consists of the choice $U_h = S^2(\mathcal{T})^d$ for the velocity space and $Q_h = S^1(\mathcal{T}) \cap L_0^2(\Omega)$ with $S^p(\mathcal{T})$ defined as in (3.4). It is well-known that the Taylor-Hood elements fulfill the discrete inf-sup condition, see, e. g., Section 10.6 of [13].

3.4.5   Equal-Order Stabilized System

Since the choice of (equal-order) piecewise linear elements for U_h and Q_h is unstable, one has to modify the system to ensure stability. The problem is from *spurious pressure modes*. These are pressure modes that are non-constant and in the null space of $b(v, \cdot) = 0$ [27, Section 3.3]. An often-used example is the "checkerboard-mode" where adjacent elements have different signs. The loss of numerical stability for equal-order methods is due to the fact that c in (3.16) is inversely proportional to the discrete inf-sup constant β, which tends to zero for mesh sizes approaching zero.

Hence some workaround for this problem has to be found. The method described in the following is a sort of Galerkin-Least-Squares (GLS) stabilization. For piecewise linear approximations in the discrete Stokes system, the stabilization terms $\delta(\nabla p_h, \nabla q)$ and $\delta(f, \nabla q)$ are added to the bilinear and linear form in (3.12), respectively. Then the FEM approximation reads: find $(u_h, p_h) \in U_h \times Q_h$ such that

$$B_h((u_h, p_h), (v_h, q_h)) = F_h((v_h, q_h)) \qquad \forall (v_h, q_h) \in U_h \times Q_h \,,$$
$$B_h((u_h, p_h), (v_h, q_h)) := B((u_h, p), (v_h, q_h)) + \delta(\nabla p_h, \nabla q_h) \,,$$
$$F_h((v_h, q_h)) := l(v_h) + \delta(f, \nabla q_h) \,.$$

The merits of this formulation are two-fold. First, B_h is coercive. Second, large gradients of the pressure are penalized. The choice of δ is crucial: δ should be large enough to gain numerical stability but at the

same time small to disturb the original problem as little as possible. Furthermore, in pursuance of making the inf-sup constant independent of h, a suitable choice is $\delta = Ch^2$, where C is some constant [48].

3.5 AXISYMMETRIC FORMULATION IN CYLINDRICAL COORDINATES

As the cavity in most pores is of approximately axisymmetric shape, cylindrical coordinates provide useful. Obviously, an off-centered molecule breaks the axisymmetry, so in this case a full 3d model is required.

Assuming the data is axisymmetric with zero angular component, the problem can be reduced to the 2d halfplane $\mathbb{R}^+ \times \mathbb{R}$, meaning that solutions will only depend on the axisymmetric cylindrical coordinates (r, z) instead of the three cylindrical coordinates (r, θ, z). For example, the 3d velocity field v is then given by (under slight abuse of notation)

$$v(x, y, z) = v(r, \theta, z) = \begin{pmatrix} v_r(r, z) \cos\theta \\ v_r(r, z) \sin\theta \\ v_z(r, z) \end{pmatrix} .$$

Thus a function depends only on r and z and $\nabla\phi = (\partial_r\phi, \partial_z\phi)$ for a scalar function ϕ and $\nabla \cdot u = \partial_r u_r + \partial_z u_z$ for a vector field u. The inner product $(\cdot, \cdot)_\Omega$ is understood as $(\phi, \psi)_\Omega = 2\pi \int_\Omega \phi\,\psi\,r\,drdz$. On the computational side, the solution of an axisymmetric PNPS system is much cheaper and faster.

For the sake of completeness, the axisymmetric weak form of the PNP and the Stokes equations is stated. First, the PNP equations in weak formulation are considered:

$$\left(\epsilon\nabla\phi, \nabla\psi\right)_\Omega - \left(F(c^+ - c^-), \psi\right)_{\Omega_f} - \left(\rho_0, \psi\right)_\Omega - \left(\rho_S, \psi\right)\big|_{\Gamma_i} = 0 ,$$

$$\left(D^+\nabla c^+ + \mu^+ c^+\nabla\phi - c^+ v, \nabla\theta^+\right)_{\Omega_f} = 0 , \tag{3.17}$$

$$\left(D^-\nabla c^- - \mu^- c^-\nabla\phi - c^- v, \nabla\theta^-\right)_{\Omega_f} = 0 .$$

Second, the weak formulation of the axisymmetric Stokes problem reads

$$
\left(\eta \nabla v, \nabla u\right)_{\Omega_f} + \left(\eta \frac{v_r}{r}, \frac{u_r}{r}\right)_{\Omega_f} - \left(\nabla \cdot u, p\right)_{\Omega_f} - \left(\frac{u_r}{r}, p\right)_{\Omega_f} +
$$
$$
+ \left((c^+ - c^-)\nabla\phi, u\right)_{\Omega_f} = 0 \, , \tag{3.18}
$$
$$
\left(\nabla \cdot v, q\right)_{\Omega_f} + \left(\frac{v_r}{r}, q\right)_{\Omega_f} = 0 \, .
$$

The weak formulation of the axisymmetric PNP equations in cylindrical coordinates (3.17) is pretty straightforward. The derivation of the weak axisymmetric Stokes problem (3.18) needs a little bit more care; for details, see [25].

3.6   ADAPTIVITY

In order to efficiently solve the equations, adaptive FEM was used. Consequently the grid is refined, where the error is large. For the error analysis of "goal" functionals and adaptive meshing strategies minimizing the error [8] is a good source of information. This section focuses on goal-oriented adaptivity and follows [8].

The goal of simulations is mostly focused on obtaining physical quantities, thus these quantities can be represented as the value of some functional J of the solution, referred to as "goal" functional. The idea behind adaptivity is either to minimize the work W needed for the computation for some given tolerance tol of the goal or to maximize the accuracy of the goal for a fixed work W.

The adaptivity process is guided by a basic SEMR algorithm:

SOLVE → ESTIMATE → MARK → REFINE .

Expanded, the SEMR algorithm reads:
   While some termination criterion is unfulfilled, repeat:

   1. Compute numerical solution for mesh,

   2. Evaluate error indicators,

   3. Mark/Select elements of mesh for refinement,

   4. Refine mesh.

For the marking of elements, Dörfler-marking was chosen. The termination criterion can be a critical amount of elements corresponding to a maximal work load or the estimated error of the goal functional being less than a tolerance tol.

For a system of PDEs it is not a priori clear which equation should be guiding the adaptation process. For the PNPS problem, the suspected regions prone to errors are near interfaces. The electrical double layers near charged boundaries are regions that give rise to large local gradients in the concentrations. This motivates the decision to let the PNP equations guide the refinement process. Indeed, an even cheaper method is to use the linear PB equation as a rough approximation for the PNP equations. As an additional bonus the solution of the PB equation also delivers an initial guess for Newton's method on PNP.

3.6.1 Goal-oriented Adaptivity

An efficient strategy to obtain accurate values for a certain functional is goal-oriented adaptivity. As in [8], the dual-weighted-residual (DWR) method is going to be presented.

Given a linear functional J, the interest is to minimize the error $J(e) = J(u - u_h) = J(u) - J(u_h)$. Here e is the approximation error of u and u_h. Let u be the solution of the model problem: find $u \in V$ such that:

$$a(u, v) = f(v) \qquad \forall v \in V, \tag{3.19}$$

where a is a continuous coercive bilinear form and l is a linear continuous functional. So u is the exact solution of the original or primal problem (3.19). As in Section 3.1, its Galerkin projection u_h is given by: find $u_h \in V_h \subset V$ such that:

$$a(u_h, v_h) = f(v_h) \qquad \forall v_h \in V_h . \tag{3.20}$$

Equation (3.19) and (3.20) together imply the Galerkin orthogonality

$$a(e, \psi_h) = 0 \qquad \forall \psi_h \in V_h . \tag{3.21}$$

For $J : V \to \mathbb{R}$ the following so-called *dual* problem has to be solved: find z and its finite element approximation z_h defined by

$$a(\phi, z) = J(\phi) \qquad \forall \phi \in V$$
$$a(\phi_h, z_h) = J(\phi_h) \qquad \forall \phi_h \in V_h .$$

Defining the residual

$$\rho(u_h)(v) := l(v) - a(u_h, v) ,$$

where $v \in V$, gives the following representation of the error

$$J(e) = a(e, z) = a(e, z - \psi_h) = \rho(u_h)(z - \psi_h) \qquad \psi_h \in V_h .$$

Here the Galerkin orthogonality (3.21) was exploited. The residual $\rho(u_h)(\cdot)$ can be regarded as a functional on V. Moreover, for a concrete tessellation $\mathcal{T}_h$ one can define cell and edge residuals R_h and r_h. Then the following a posteriori error representation can be established

$$J(e) = \rho(u_h)(z - \psi_h) = \sum_{K \in \mathcal{T}_h} \left((R_h, z - \psi_h)_K + (r_h, z - \psi_h)_{\partial K} \right) . \quad (3.22)$$

The error $J(e)$ can also be expressed in terms of element residuals ρ_K and weights ω_K for $K \in \mathcal{T}_h$:

$$|J(e)| \leq \eta_\omega := \sum_{K \in \mathcal{T}_h} \rho_K w_K ,$$

$$\rho_K := \left(\|R_h\|_K^2 + h_K^{-1} \|r_h\|_{\partial K}^2 \right)^{1/2} ,$$

$$w_K := \left(\|z - \psi_h\|_K^2 + h_K \|z - \psi_h\|_{\partial K}^2 \right)^{1/2} .$$

For a more explicit example see the next Subsection 3.6.2, where this method is applied on the linear PB problem.

The remaining goal is to develop an accurate yet cheap way to compute $J(e)$. Just plugging a Galerkin solution $z_h \in V_h \subset V$ as an approximation to z into the a-posteriori error $J(e)$ in (3.22) is useless as by Galerkin orthogonality $J(e)$ vanishes. Thus, more elaborate methods must be used for the numerical approximation of z. A higher-order interpolation method is considered on z, outlined in Section 4.1 of [8] for quadrilateral meshes and extended to tessellations in [62].

The main idea behind this method is to compute the Galerkin approximation z_h, extrapolate z_h patch-wise on a higher-order function space $W_h \supset V_h$ yielding the higher order interpolation $E z_h \in W_h$. So, the method basically consists of the two steps:

1. *Lifting*, where the element-wise solution is fitted on a patch by a least-squares approximation in a higher order space, and

2. *Smoothing*, where the (possibly multivalued) higher order function is averaged at shared degrees of freedoms (DOFs).

The method is illustrated in Figure 3, which is taken from [62] where also the details for this method can be found.

Thus, the error in J can be approximated via an extrapolated dual solution

$$J(e) = J(u - u_h) = \rho(u_h)(z) \approx \rho(u_h)(E z_h). \quad (3.23)$$

In [8] it is demonstrated that the patch-wise biquadratic interpolation I_{2h}^2 of the bilinear Ritz projection z_h leads to the estimate

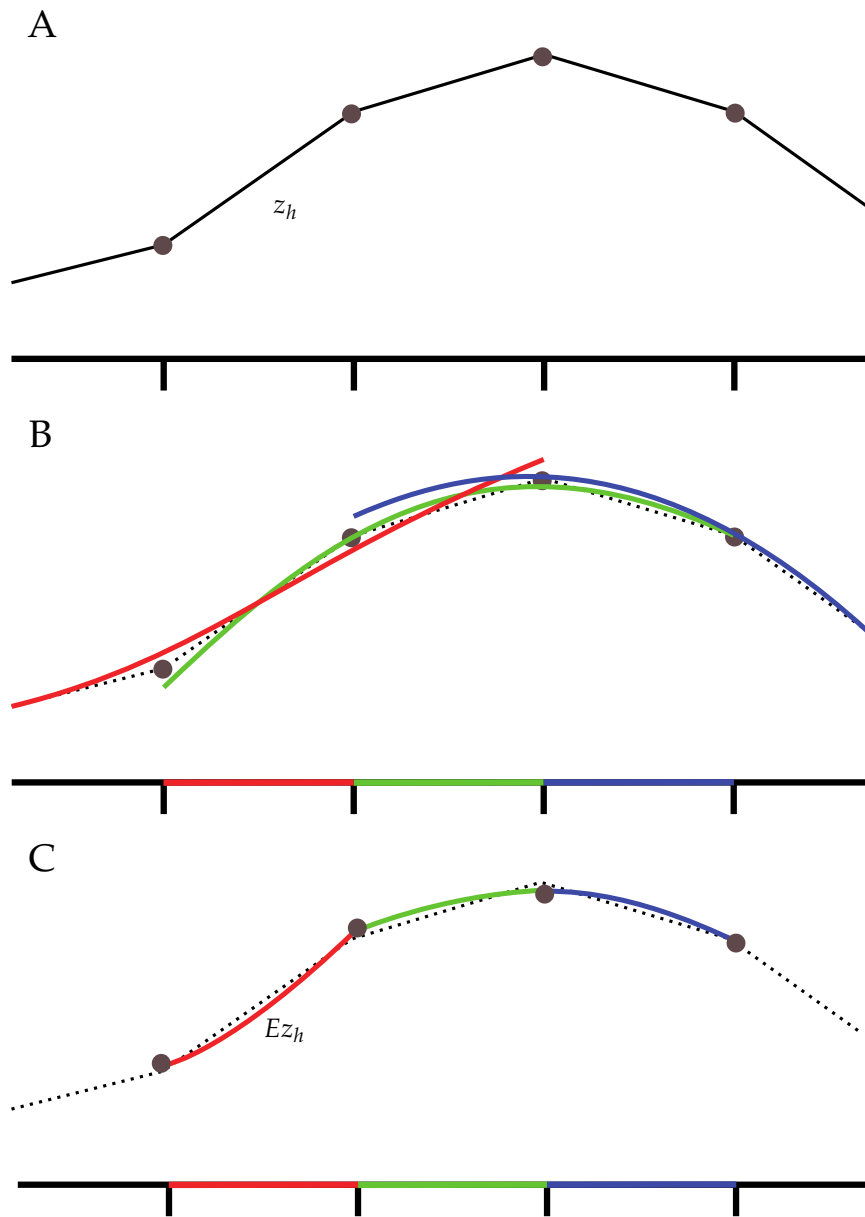$$J(e) = \rho(u_h)(I_{2h}^2 z_h - z_h) + \mathcal{O}(h^3) ,$$

Figure 3: Illustration of the process of lifting and smoothing. The figure is adapted from [62]. Subfigure A shows a piecewise linear approximation z_h, which is then lifted in Subfigure B and subsequently smoothed in the bottom Subfigure C.

where some generous assumptions were granted.

As a remark, in [62] the emphasis is on proposing an automated way for goal-oriented error control and not on examining the theoretical basis of this method. The legitimacy of this method is demonstrated on a set of problems.

In this section conforming Galerkin, i.e. $V_h \subset V$, was assumed. If, like in our problem setup, curved boundaries are present, an additional source of error is introduced, as the space V_h is not conforming anymore. As a side note, the DWR method can also be extended to nonlinear problems, see Chapter 6 of [8].

3.6.2   Prerefinement with the PB Equation

To make the computation of the mesh indicators, which guide the refinement process, computationally cheap the PNP equation was approximated by the linear PB equation with homogeneous Dirichlet BCs and interface conditions (2.11). This means that the adaptation process was guided by a goal functional composed of the F_{el} and terms based on the electrical field inside the pore.

To provide a concrete example of the above abstract goal-adaptivity, consider the linear PB equation (2.24). An explicit form for the residuals is obtained by cellwise integration by parts and results in

$$
\begin{aligned}
\rho(\phi_h)(z - \psi_h) = \sum_{K \in \mathcal{T}_h} \big\{ &(\rho_0, z - \psi_h)_K + (\epsilon \Delta \phi_h, z - \psi_h)_K \\
&- \widehat{\lambda_D}^{-2} (\chi_f \phi_h, z - \psi_h)_K + (\rho_S, z - \psi_h)_{\partial K} \\
&- (\epsilon \nabla \phi_h \cdot n, z - \psi_H)_{\partial K} \big\} \, ,
\end{aligned}
$$

where $\widehat{\lambda_D}^2 = 2 F c_0 e / (k_B T)$ and χ_f is the indicator function of the fluid domain. Thus, for K and e being a cell and an edge of the triangulation $\mathcal{T}_h$, respectively, cell and edge residuals R_h and r_h read

$$
R_{h|K} := \rho_0 + \epsilon \Delta \phi_h - \widehat{\lambda_D}^{-2} \chi_f \phi_h \, ,
$$

$$
r_{h|e} := \begin{cases} 0 \, , & \text{if } e \subset \partial \Omega \, , \\ \frac{1}{2}(\rho_S - [\epsilon \nabla \phi_h \cdot n]) \, , & \text{if } e \subset \Gamma_I \, , \\ \frac{1}{2}[\epsilon \nabla \phi_h \cdot n] & \text{else} \, . \end{cases}
$$

Finally, an a posteriori error representation of the form (3.22) can be derived:

$$
J(e) = \sum_{K \in \mathcal{T}_h} \big\{ (R_h, z - \psi_h)_K + (r_h, z - \psi_h)_e \big\} \, .
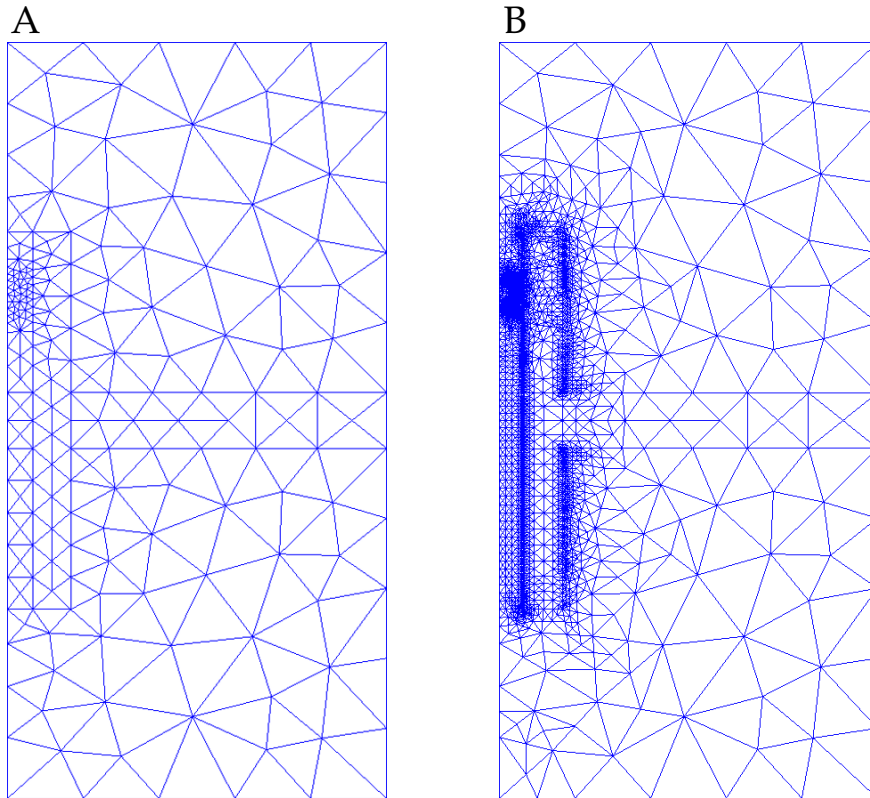$$

A   B

Figure 4: Two meshes of the pore geometry (P3) with a molecule inside. Subfigure A shows a base mesh with 377 elements. Subfigure B shows an adapted mesh with 9603 elements. The mesh was refined with the method described in Section 3.6.2.

First, the effect of goal-oriented adaptivity on the meshes is shown in Figure 4. Second, the benefit of using goal-oriented adaptive mesh refinement over residual-based or uniform refinement can be seen in Figure 5. This figure also shows the need for fine meshes, as only fine meshes produce accurate enough physical quantities of interest.

3.7 Computation of the Physical Quantities

The accurate computation of the physical goal quantities is challenging, especially for the forces in the full 3d (non-axisymmetric) case. The computation of gradients on surface integrals is numerically not very stable, as shown for lift and drag coefficients in [8]. Hence volume integrals are preferred. The current was evaluated as a volume
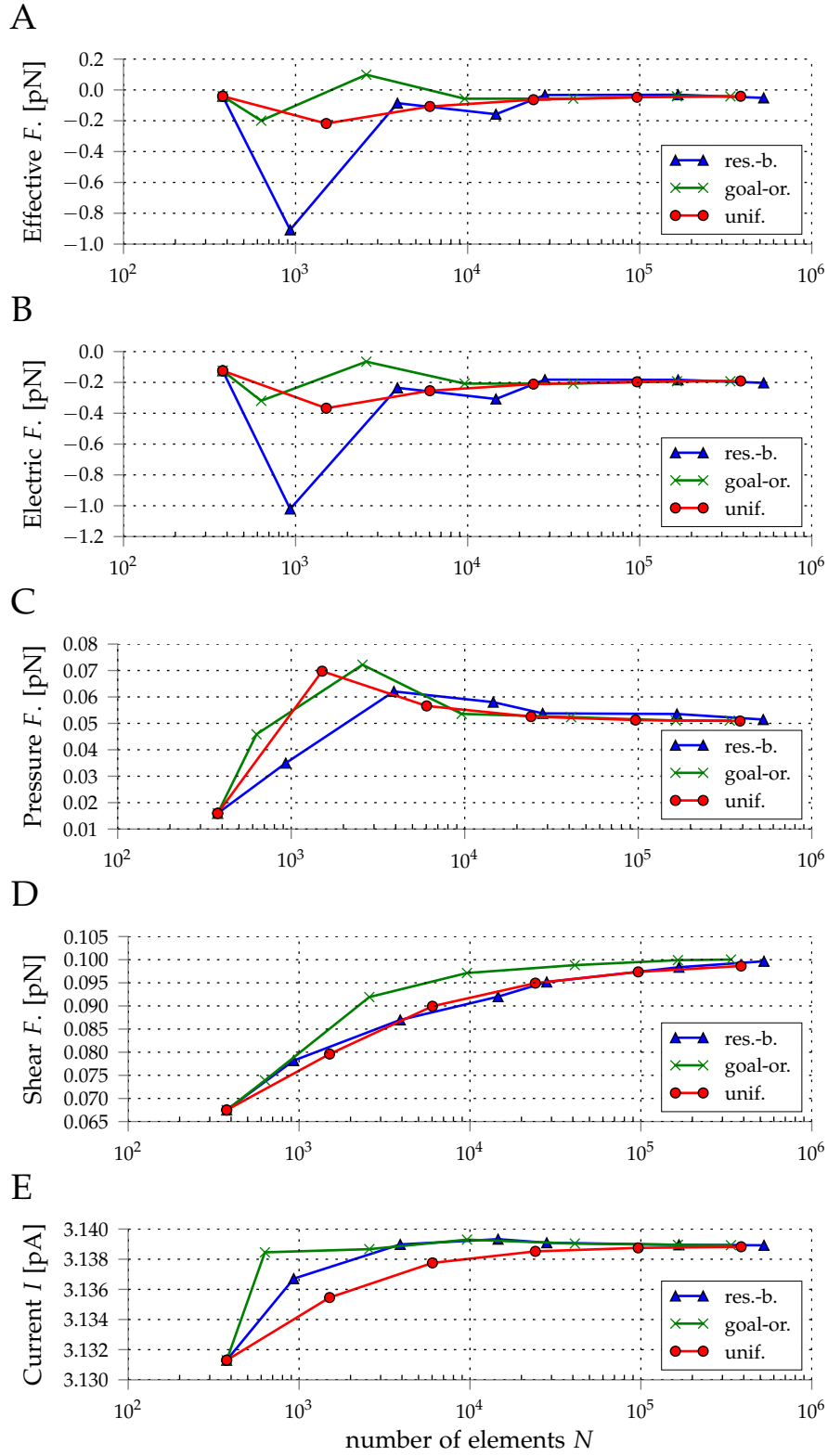
A

B

C

D

E

Figure 5: Convergence of forces and current over the total number of triangles N for residual-based, goal-oriented and uniform refinement.
A. Effective driving force F_{eff} (2.15). B. Electric force F_{el} (2.16). D. Viscous stress force F_{shear} (2.18). C. Pressure stress force F_{p} (2.19). E. Current I (2.20).

integral of a pore subdomain and subsequently divided by its length in *z*-direction.

Considering the forces acting on the molecule, the bare electric force is already a volume integral, thus the drag force remains the only surface integral. In order to achieve accurate force calculations, the adaptive approach described in Section 3.6 was necessary for the full 3d model for two reasons. First, as pointed out in Section 3.4.3, the Stokes system is expensive. Second, the adaptive procedure yields better values for the forces and the current at a lower number of triangulation elements, which can be seen in Figure 5. Still, small mesh sizes in the vicinity of the molecule and of charged pore walls are crucial for accurate goal quantities. In Figure 5 one can see that the number of elements N has to be at least 10^4 in order to obtain reliable values for the forces. This number corresponds to a mesh size of approximately 10^{-11} m. However, in 3d such small mesh sizes result in huge linear systems and are at the computational limit of current workstations.

3.8   ITERATIVE SOLVERS

Since the most time-consuming step in FEM is usually the solution of the large sparse linear system, one is interested in efficient methods. In FEM the stiffness matrices are typically sparse. While direct sparse solution methods are the safest choice regarding robustness, they are expensive with respect to time and memory. This is even more true for 3d models. Iterative methods are much faster; however, a good knowledge of the structure of the underlying system is often needed. Without preconditioning, iterative solvers often lack robustness and one might end up in an unsatisfactory trial and error process. Thus, preconditioning is often the key to an efficient and fast convergence of iterative solvers [63].

For the linear problem arising from Newton's method on the PNP equations a Krylov subspace method, namely BiCGstab, together with a preconditioner was used. However, if adaptive mesh refinement is used the stiffness matrix might become ill-conditioned. This gives rise to difficulties for iterative methods [31, p. 4.4]. This phenomenon was also numerically observed.

Iterative solvers for the Stokes problem have to be designed with care due to the saddle point structure [27]. In the simulations, a direct method was used as the stiffness matrix of the Stokes problem can be reused in every step of the hybrid iteration, as mentioned in Section 3.2.

3.9   IMPLEMENTATION AND MESH GENERATION

In the last section of this chapter the implementation is described and the used software packages are listed. As a part of this thesis, a Python package named `nanopores` was written together with Gregor Mitscha-Baude and Benjamin Stadlbauer. The aim of the package were simulations of nanopores with different geometries. Due to the modular approach it is versatile and not only applicable to nanopores and the PNPS system, but easily extendable to a wider class of PDEs. The package makes heavy use of Gmsh and FEniCS.

FEniCS is a free and open-source software package aimed at the automated solution of PDEs [50]. It consists of several core components, namely DOLFIN [51], FIAT [45], FFC [52], UFL [3], UFC [4] and SyFi [5]. The API of FEniCS is based on a C++/Python library. The Python interface allows intuitive and object-oriented scripting in Python and is semi-automatically generated by SWIG. This is the reason why the `nanopores` package was written in Python.

Gmsh is a three-dimensional mesh generator [30] aimed at fast and light mesh generation. It is written in C++ and features a built-in CAD engine and visualization. Gmsh uses a "bottom-up" approach, meaning that one first has to define points. Then one has to connect these points with lines, then these lines can be extruded to create surfaces and so on. Thus, the description of the geometry is done by its boundary representation. To provide good initial meshes, mesh size fields were used to control the mesh size appropriately. Hence in the vicinity of curved boundaries, the mesh size was decreased to better feature the underlying geometry.

As Gmsh has its own scripting language another Python package, namely `py4gmsh`[1] by Nico Schlömer, proved very helpful. Roughly speaking, `py4gmsh` translates Python code into gmsh code, thus facilitating an efficient and comprehensive implementation in Python.

---

[1] https://github.com/nschloe/python4gmsh

4

RESULTS AND DISCUSSION

In this chapter, simulation results are presented and compared with experiments and other simulations. First, in Section 4.1 the simulated nanopore geometries are listed. In Section 4.2, the geometry parameters of each of the presented pores are specified and notes on crucial physical parameters are given. The limitations of the model equations are discussed in Section 4.3. The effects of geometry and physical parameters on the conductance are discussed in Section 4.4. Also, the simulations are compared with experiments to validate the model. In Section 4.5, the calculated force is shown to coincide with a reference solution. Lastly, in Section 4.6, more simulation results are presented. Concentrations and solvent flow fields are shown. Current-voltage (IV) curves for different pores are discussed and an effective force field is shown.

4.1 Nanopore Geometries

Simulations were restricted to four different types of nanopores. The selection is based on nanopores examined in experiments. These four different nanopore setups are abbreviated as P1, P2, P3 and P4:

(P1) A solid-state nanopore with an 100 nm long DNA strand inside as presented in [54], cf. Figure 6A.

(P2) A solid state nanopore designed for stochastic sensing as presented in [70], cf. Figure 6B.

(P3) A DNA origami nanopore consisting of six DNA strands as presented in [14], cf. Figure 6C.

(P4) A biological heptameric staphylococcal α-hemolysin nanopore, see [7] or [68], cf. Figure 6D.

Figure 6 shows the geometries of the four different nanopores. The implemented geometries are an axisymmetric approximation of the complicated realistic geometries.
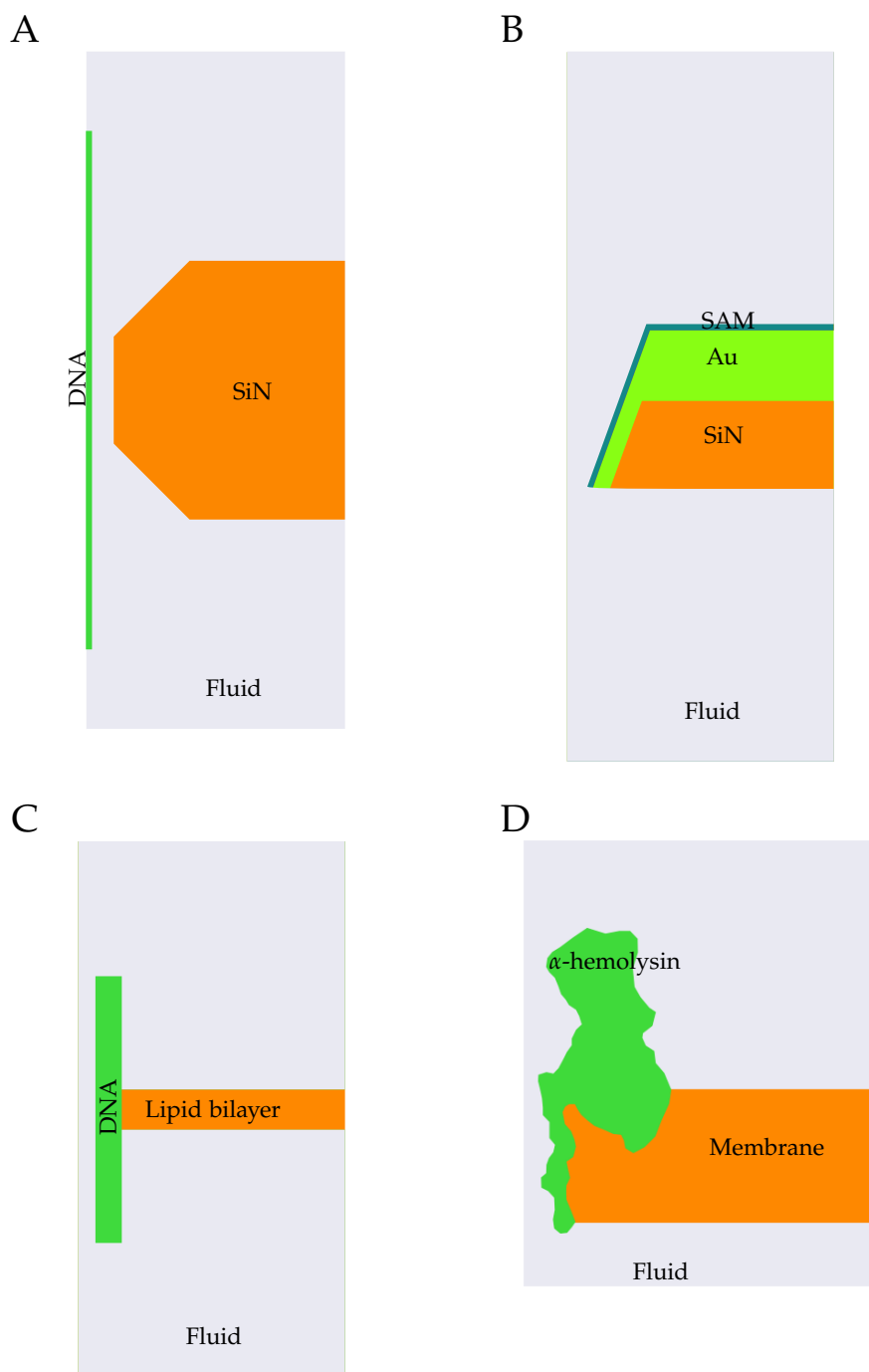
Figure 6: Cross-sections of the nanopores used for simulations. They are not shown at the same length scale.
A. Solid-state nanopore (P1). B. Solid-state nanopore (P2). C. DNA origami nanopore (P3). D. α-Hemolysin nanopore (P4).

4.2 PARAMETERS

4.2.1 Geometrical Parameters

(P1) The geometry of the pore in [54] has an hourglass shape. The diameter ranges from 5 to 20 nm. A DNA strand of one Kuhn length, i.e. 100 nm, is assumed to reside inside the pore. The exact geometry parameters can be found in Table 1.

Table 1: Geometry parameters (P1)

Inner pore radius	5.0 nm
Outer pore radius	20.0 nm
Inner pore length	20.0 nm
Membrane thickness	50.0 nm
DNA length	100.0 nm
DNA radius	1.1 nm

(P2) The geometry of the pore in [70] is conical. The lower diameter of the pore varies from around 20 nm up to 45 nm. The aperture angle was experimentally determined by TEM tomography to be $40°$. The 50 nm SiN membrane was coated with a 10 nm Ti and a 30 nm Au layer, resulting in a total membrane thickness of 90 nm. For simplicity the Ti layer was neglected in the pore model. Simulations are presented before and after formation of a self-assembled monolayer (SAM) layer, thus the SAM layer is removed or included accordingly. Table 2 lists the geometry parameters of this pore.

Table 2: Geometry parameters (P2)

Effective pore radius	13 nm
Aperture angle	40 °
SiN membrane thickness	50 nm
Au membrane thickness	40 nm
Au thickness inside pore	10 nm
SAM layer thickness	3 nm

(P3) The geometry of the pore in [14] is a DNA barrel consisting of six duplexes connected via crossovers. The DNA strands are chemically modified to produce structurally stable lipid bilayer

spanning nanopores. The pore was approximated by a hollow cylinder. The geometry parameters are given in the following Table 3.

Table 3: Geometry parameters (P3)

Pore radius	1.0 nm
Barrel outer radius	2.5 nm
Pore length	15.0 nm
Membrane thickness	2.2 nm

(P4) The geometry consists of an α-hemolysin pore spanning a membrane. The α-hemolysin boundary was approximated by a total number of 96 point coordinates. The inner pore radius ranges from 0.6 to 2.0 nm. The pore length is 10 nm.

If simulations with a molecule inside the pore are run, a molecule radius of $r_\mathrm{M} = 0.55$ nm is used if not specified otherwise.

4.2.2   Physical Parameters

In this section, the physical parameters used within the simulations are listed. Tables of the fundamental physical constants and material constants can be found in the Appendix, Table 4 and Table 5, respectively.

- Surface charge:
  The surface charge of some materials depends on the pH value of the solution. In [39] the membrane potential was studied for SAM in a 1 mM KCl solution with different pH values. For a pH value of 7.5 the SAM surface potential is found to be approximately -22 mV and for a pH of 9.0 it is -49 mV. Then the surface charge can be calculated by the Grahame equation

$$\sigma = \frac{2\epsilon k_B T}{e\lambda_D} \sinh\left(\frac{e\psi}{2k_B T}\right) , \tag{4.1}$$

  where

$$\lambda_D = \left(\frac{\epsilon_0 \epsilon_s k_B T}{2eFc_0}\right)^{1/2} \tag{4.2}$$

  is the Debye length. The Debye length was determined as 9.63 nm. This results in surface charges $\sigma \approx -1.6$ mC/m^2 and $\sigma \approx -4.1$ mC/m^2.

For the surface charge of SiN an approximate value of -22 mC/m^2 was used in the simulations, which agrees with a pH value of 8.0, cf. [54]. In [28] the surface charge and zeta potential of SiN nanopores and their effects on protein translocation was studied in dependence of the pH value. The surface charge of the Au area in (P2) was varied. However, for large ion concentrations the surface charge may rise, as pointed out in [10] and [67] for silica surfaces.

The charge of the lipid bilayer was assumed to be zero in (P3) and (P4). Regarding the charge distribution on the DNA surface in (P3), only the side boundaries of the strands were charged. The top and bottom surfaces were assumed to be neutral.

- Protein charge:
  The protein charge Q is stated explicitly for each simulation.

- Ionic concentration:
  The bulk concentration of the ions ranged from 400 mM up to 1000 mM in the experiments. The simulations were restricted to the case of KCl solutions, i. e. monovalent K$^+$ and Cl$^-$ ions.

- Permittivites:
  The relative permittivities are given in Table 5, except for the permittivity of the α-hemolysin pore, where a relative permittivity of 12.0 was assumed.

- Diffusivity, mobility and conductance:
  Mobility and diffusion are related to each other via the Einstein-Smoluchowski relation (2.9).

  A comparison between measured bulk conductance values and local conductance values given by (2.13) with physical parameters inserted (as specified in Table 4) suggests that one has to correct the calculated conductance values [61]. Especially for high salinities the experimentally determined conductance deviates from the local conductance, as the latter depends linearly on the concentration, which opposes the nonlinearity in the measurements.

  Furthermore, the mobility and hence the diffusivity vary in small pores; this issue is also discussed in the sections below. Thus, in the validation process of (P3) and (P4) the diffusivity was reduced to achieve agreement between simulation and data.

4.3   LIMITATIONS OF THE MODEL EQUATIONS

Before proceeding to the results of the simulations, some notes on the known limitations of our model equations are presented.

Since the Poisson-Nernst-Planck (PNP) equations are derived from the Boltzmann equation under certain assumptions, they suffer from the inherent limitations of these assumptions. These assumptions include point-like particles and a Maxwellian distribution for the momenta of the ions. The Maxwellian distribution corresponds to thermally equilibrated particles, hence the ion concentrations are not velocity-dependent. The Maxwellian distribution is an appropriate model for small momenta. For large applied voltages, which result in large momenta, the model is no longer adequate, see Heitzinger et al. [34].

In [33], a diffusion-type equation was derived for confined structures, e.g. nanopores or ion channels. There, the original Boltzmann equation for three spatial and three momentum variables was reduced to a diffusion-type equation depending only on the position of the particle, the local energy and time.

The PNP model tends to overestimate ion concentrations at high voltages. Thus, Kilic et al. proposed modified PNP equations in [44], which were computationally investigated in [16]. The modification includes a term accounting for finite size effects because the PNP equations treat ions as idealized mathematical points. These finite size effects lead to a maximum concentration c_{max}, a so-called steric limit, which is reached if the voltage is a few times higher than the thermal voltage U_T, see [43].

As stated in [55], the PNP model furthermore neglects ion-ion correlations and the dielectric response of the system to an ion. In other words, a single discrete charges in a high dielectric medium experiences a strong image charge, in the vicinity of the boundary to a low dielectric medium. This repulsive effect is largely lost due to the implicit mean-field approximation in the PNP equations.

That the PNP model neglects forces arising from dielectric boundaries near interfaces is also pointed out in [59], where ionic diffusion in confined geometries is investigated and a so-called conditional PNP system (C-PNP) is derived. In [20] PNP equations with an additional term to include dielectric self-energy are proposed and the obtained results are compared with BD simulations for ion channels. However, their new model only agrees well for certain pore radii, especially for very small pores or wide pores with a radius bigger than two Debye lengths. The invalidity of continuum models for such small pores is demonstrated in [19].

In the model used for the simulations behind this thesis, charges were included either as constant surface charges or as constant volume charges which is a main limitation for some effects, e. g. ion current rectification (ICR) in pore (P4). Also, polarity of molecules is excluded which makes effects such as solvation shells beyond this model.

Another point worth a discussion is the fact that the membrane and the DNA are totally excluded from ion and electron transport.

The Stokes equations also suffers from small weaknesses. For example, the incompressibility condition might not hold in the vicinity of nanopores as pointed out in [56].

4.4 Conductance Validation

In this section the conductance, the inverse of the resistance, of nanopores was studied. As a first step, the conductance of pore (P3) was analyzed in detail. Furthermore, also pore (P2) was studied.

The conductance of the pore was simulated for different DNA surface charges and different ionic diffusion constants in the pore. The results are displayed for the absolute physical values and relative DNA damping factors in Figure 7B and Figure 7A, respectively. That these damping factors are reasonable is explained in the following paragraphs. In the figures, the experimentally determined conductance from [14] is marked by a contour line at 395 pS.

Seifert et al. point out that there might exist two conductance states, one high conductance state and one low conductance state [65]. Referring to [65], the above conductance value of 395 pS corresponds to a low conductance state. The values given there for DNA nanopores mounted on nanopipettes are 1.5 nS and 0.24 nS for the high and low conductance state, respectively. A numerical investigation of this voltage-dependent conductance switching behavior is beyond the scope of this thesis.

The conductance analysis of (P3) shows that in order to attain agreement between experiment and simulation, the diffusion and the bare surface charge values have to be lowered. Since for a single conductance value there exists a manifold of different possibilities regarding the effective diffusion and surface charge constant, values for the charge found in the literature provided guidance. In [67] and [42], an effective charge reduction of 71% and 75%, respectively, is proposed.

In Ho et al. [36] it is shown for a SiN nanopore that the mobility is not constant in the pore. This is backed by molecular dynamics (MD) simulations for small nanopores. Especially at the pore walls,
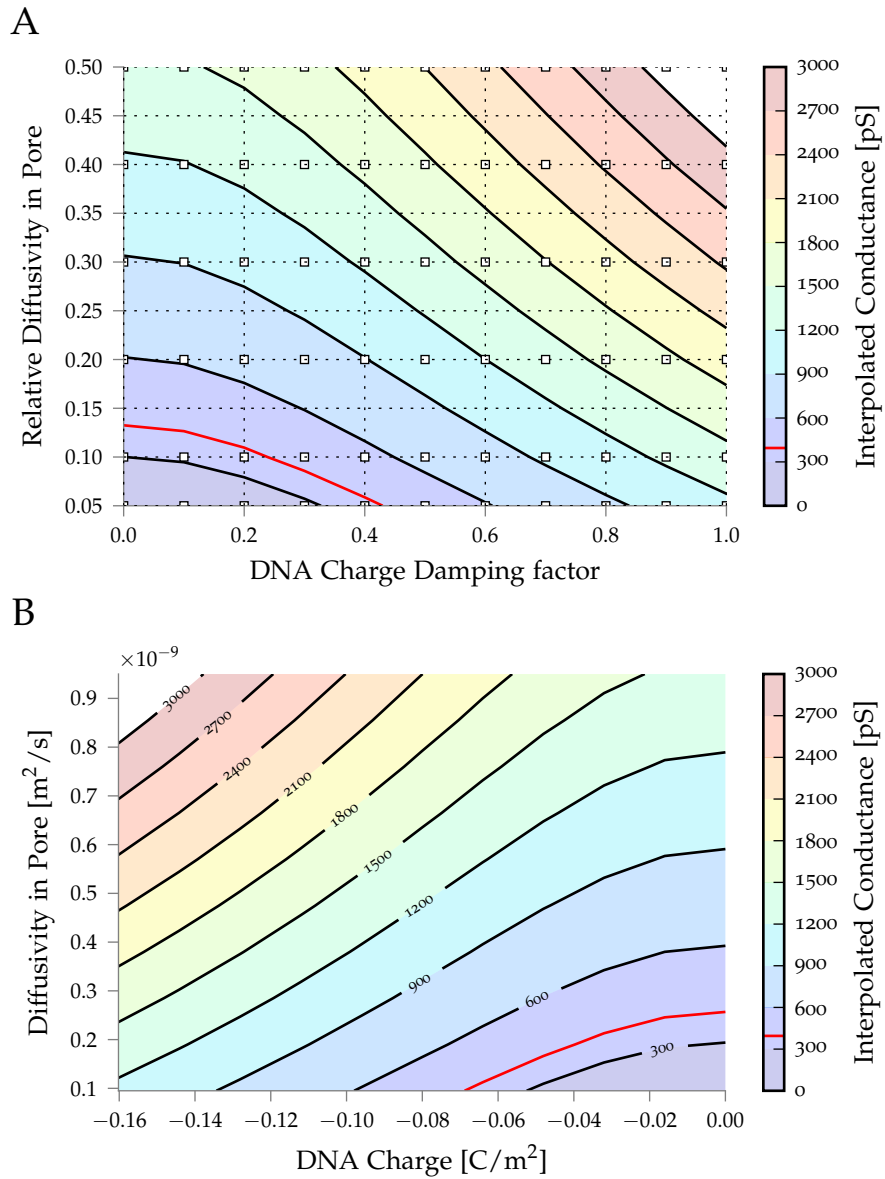
A

B

Figure 7: Interpolated conductance of (P3). The conductances were obtained by taking means of respective IV curves.
A. Interpolated conductance of (P3) with relative damping factors. The white squares mark the interpolated data points. B. Interpolated conductance of (P3) in dependence of absolute pore diffusivity and DNA surface charge.

the ion mobilities are reduced. There, the mobility of counterions is quite small, down to 10 to 20% of the bulk value, see [72] or [36]. Roughly speaking, counterions "stick" to the charged surface. This strengthens the assumption of a smaller averaged mobility throughout the pore. As by (2.9) the mobility is related to the diffusivity; also, the mobility is lowered inside the pore. Thus, in the following simulations of pore (P3) a value of 0.48 mC/m^2 is used for the surface charge and in Figure 7B the diffusivity D is set to 0.19 m^2/s.

Summarizing, the diffusion coefficient inside the small nanopore (P3) was adopted for the simulations in order to ensure valid currents.

Also, pore (P2) was analyzed regarding conductance. This pore is much wider than pore (P3), thus bulk behavior is dominant. In Wei et al. the pore diameter was estimated through a simple pore resistance model for conical pores given by (2.14) [70]. The pore diameter is afflicted with errors coming from this simple approximation, where edge effects and electrical double layers are neglected.

A comparison of this simple model with the simulated resistance provided by the more elaborate Poisson-Nernst-Planck-Stokes (PNPS) model shows that the simulated resistance is higher. In the simulations bulk values for the diffusivity and mobility are used inside the pore, if one would lower them this would increase the bias between the simple and the PNPS model even more.

Figure 8 shows the conductance dependence of the pore diameter with and without a SAM layer. As the effective pore diameter is decreased by the SAM layer, the ionic current decreases as well. Thus the resistance of the pore grows with decreasing diameter. In this figure the membrane surface charge inside the pore was also varied. For highly charged membranes the resistance converges to the one predicted by the simple model. The simulations suggest that the nanopores fabricated are not as small as stated in Wei et al. Indeed, based on the PNPS model, the pore diameter at the tip would be enlarged by a factor of around 1.25, depending on the membrane surface charge inside the pore.

4.5 VALIDATION OF THE EFFECTIVE DRIVING FORCE

In order to verify the computation of the effective driving force F_{eff}, it was analyzed for the DNA in (P1). As in Lu et al. [54], the surface charge of the membrane was ranged from -60 to 0 mC/m^2. The values given in [54] are also simulated with the PNPS model and are not determined in experiments. But the simulated values given in this
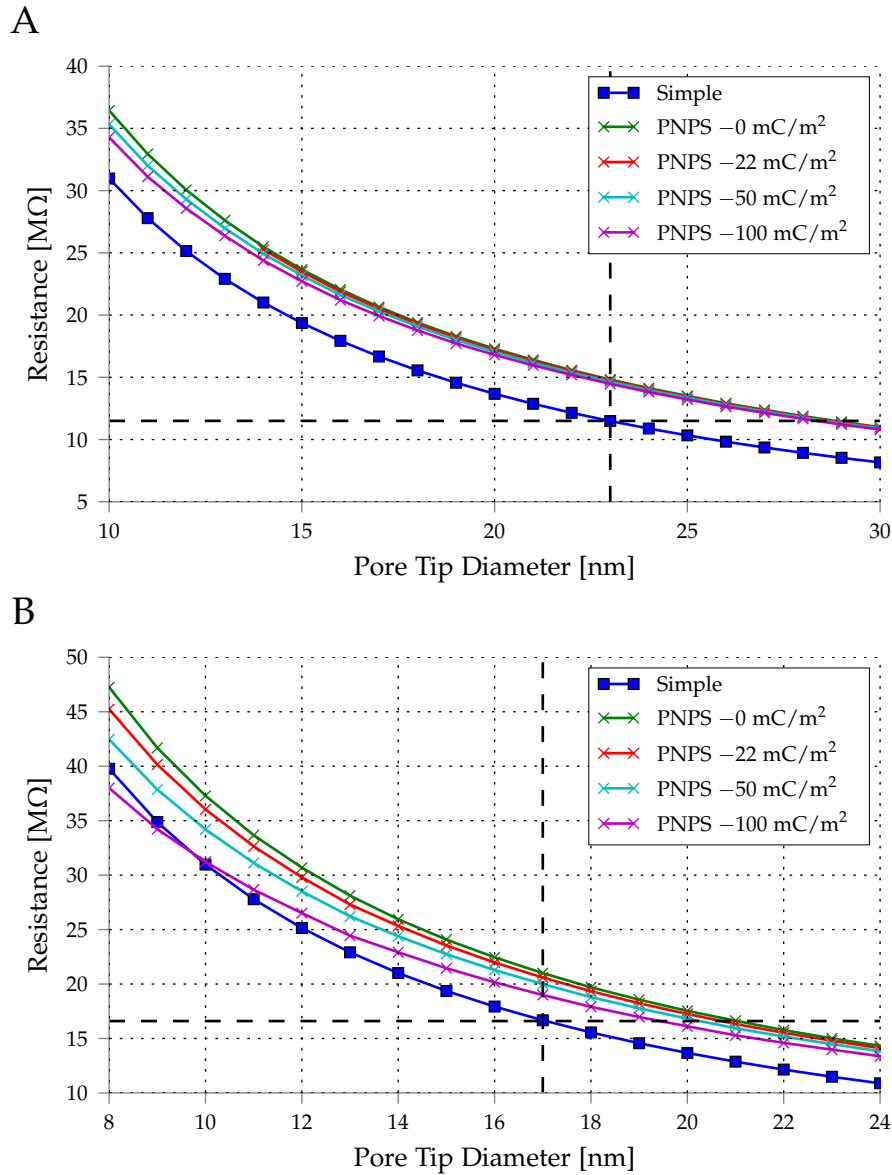
A

B

Figure 8: Resistance of pore (P2) in dependence on the pore tip diameter. Resistance levels were obtained at a biased voltage of 200 mV and bulk concentrations of 400 mM as specified in the supplementary information of [70]. The dashed lines mark the diameters and resistances given there. The simple resistance model is marked by squares. PNPS simulation results are marked by x-marks.

A. Simulation results without a SAM layer for different membrane charges of the gold layer inside the pore.

B. Simulation results with a SAM layer for different membrane charges of the SAM layer inside the pore.
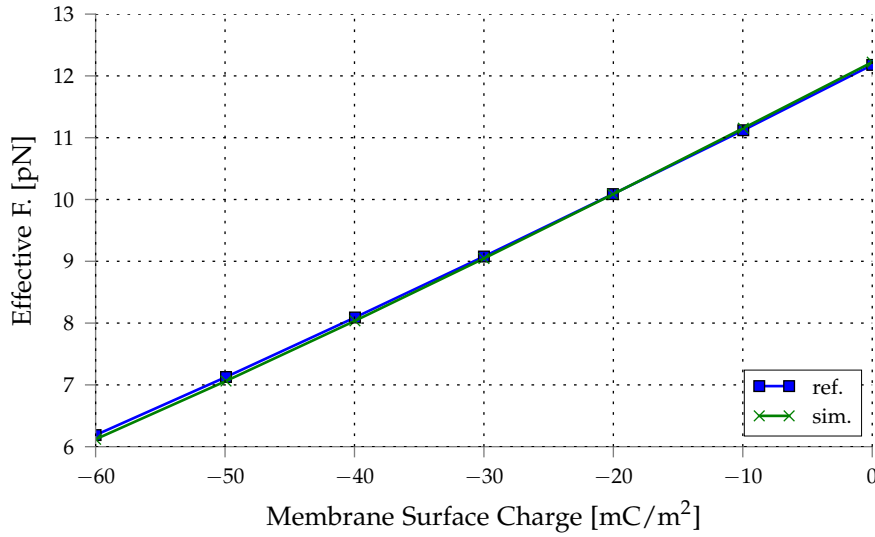
Figure 9: Effective driving force in dependence of membrane surface charge. Simulated values are compared with values given by reference [54]. In [54], the effective driving force is also simulated by the PNPS model.

reference were validated with experiments. The effect of the surface charge on the driving force can be seen in Figure 9.

The agreement between the reference values and the simulated values of the effective force are very good. The small discrepancy can be explained by the use of differently refined meshes and slightly different geometries, e. g. sharp corners were rounded off. The bare electric force is calculated by $F_{bare} = \sigma_{bare} \Delta \phi$, where $\sigma_{bare} = 136.2 \text{ mC/m}^2$ is the line charge density of the DNA and $\Delta \phi$ is the potential drop on the DNA molecule, as stated in [54]. To make the results comparable, in this pore setup (P1) the electric force F_{el} was not computed by (2.16) but by the surface integral

$$F_{el} = - \int_{\partial DNA} \sigma_{bare} \nabla \phi \, ds \, .$$

4.6 SIMULATION RESULTS

4.6.1 Solvent Flow and Ionic Concentrations

In this section, simulation results of the ionic and the solvent flow are presented. A comprehensive insight into the ion distribution and the solvent flow field inside and outside the pore is given by Figure 10 and Figure 11. Clearly, the concentrations reach their maxi-
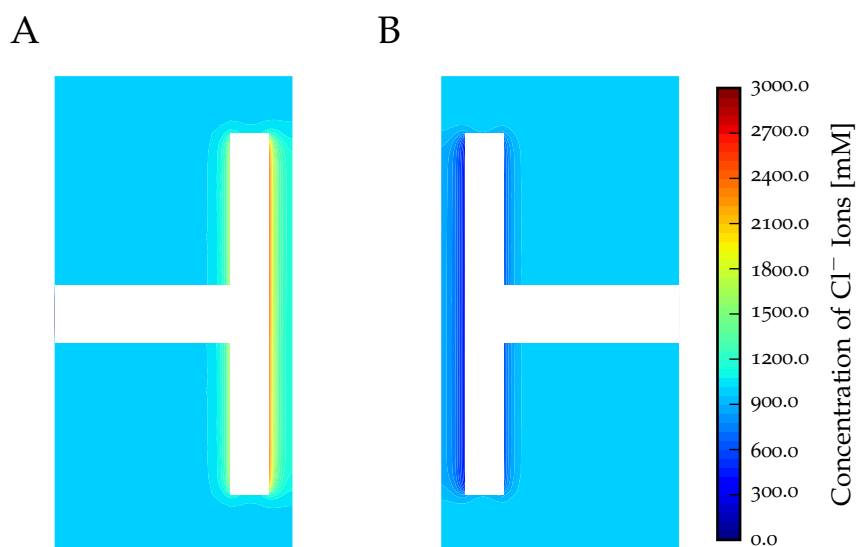
A

B

Figure 10: A color plot of the concentrations for pore (P3). The plotted domain is 10×20 nm.
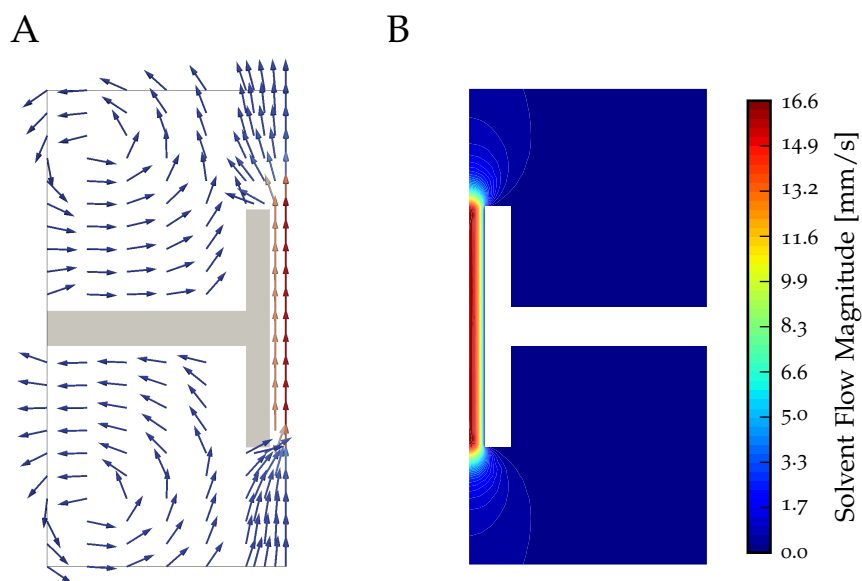A. Concentration of positive K^+ ions. B. Concentration of negative Cl^- ions.

A

B

Figure 11: The simulated velocity for pore (P3).
A. Velocity field. B. Flow magnitude.

mum and minimum near the charged surface. One can see that the cross-sectional velocity profile remains relatively unchanged inside the pore. The maximal velocity is reached at the pore axis. For absolute values consider the cross-sectional plots in Figure 12. Eddies form in the reservoir, which was also observed in [56]. Moreover, the solvent only experiences a significant acceleration in the vicinity of the pore since there charges of coions and counterions do not cancel out. As can be seen in Figure 12, the concentration of counterions inside the pore is always greater than the concentration of coions.

In Figure 12 cross-sectional plots of the concentrations and the fluid velocity field for the pore (P3) are shown. For the plots a voltage of 20 mV was applied. Recall that a reduced DNA surface charge and a lower ionic diffusion inside the pore was assumed, i.e. $\sigma = 48$ mC/m^2 and $D = 0.19$ m^2/s.

The velocity profile of the flow decreases with the pore radius due to the no-slip condition on the fluid-solid interface. The maximum velocity 0.0008 m/s is reached at the pore center. Clearly, as the ions are accelerated by the electric field they are faster on average than the water molecules, which gain their momentum through interaction with the ion molecules.

4.6.2 Current-Voltage Curves

An essential characteristic of a nanopore is its current-voltage (IV) curve. In experiments, IV curves are obtained by measuring the current while sweeping the applied voltage. Thus, an aim was to quantitatively reproduce IV measurements.

In Figure 13 the IV curve and the current components of the pore (P3) are shown. Since the pore is axisymmetric and symmetric with respect to the xy-plane due to its cylindrical shape the diffusive current flux vanishes. This is different from pore (P2).

Due to the conical shape of pore (P2) there is always a diffusive current if the pore membrane is charged, as can be seen in Figure 14B. The convective current component is nearly zero. Drift and diffusive current cancel at no applied voltage. In Figure 14 the tip diameter used in the simulations is 1.25 times bigger than stated in the experiments in [70]. A surface charge of -22 mC/m^2 was set on the whole membrane boundary. In the first subfigure the IV curve is plotted against a linear fit of the resistance given in the supplementary material of [70]. Unfortunately, no IV curve with actual experimental data is provided for this pore. As outlined in the introduction, the effects of ICR, i.e. $I(+V) \neq -I(-V)$, can be seen for this pore, since it is of
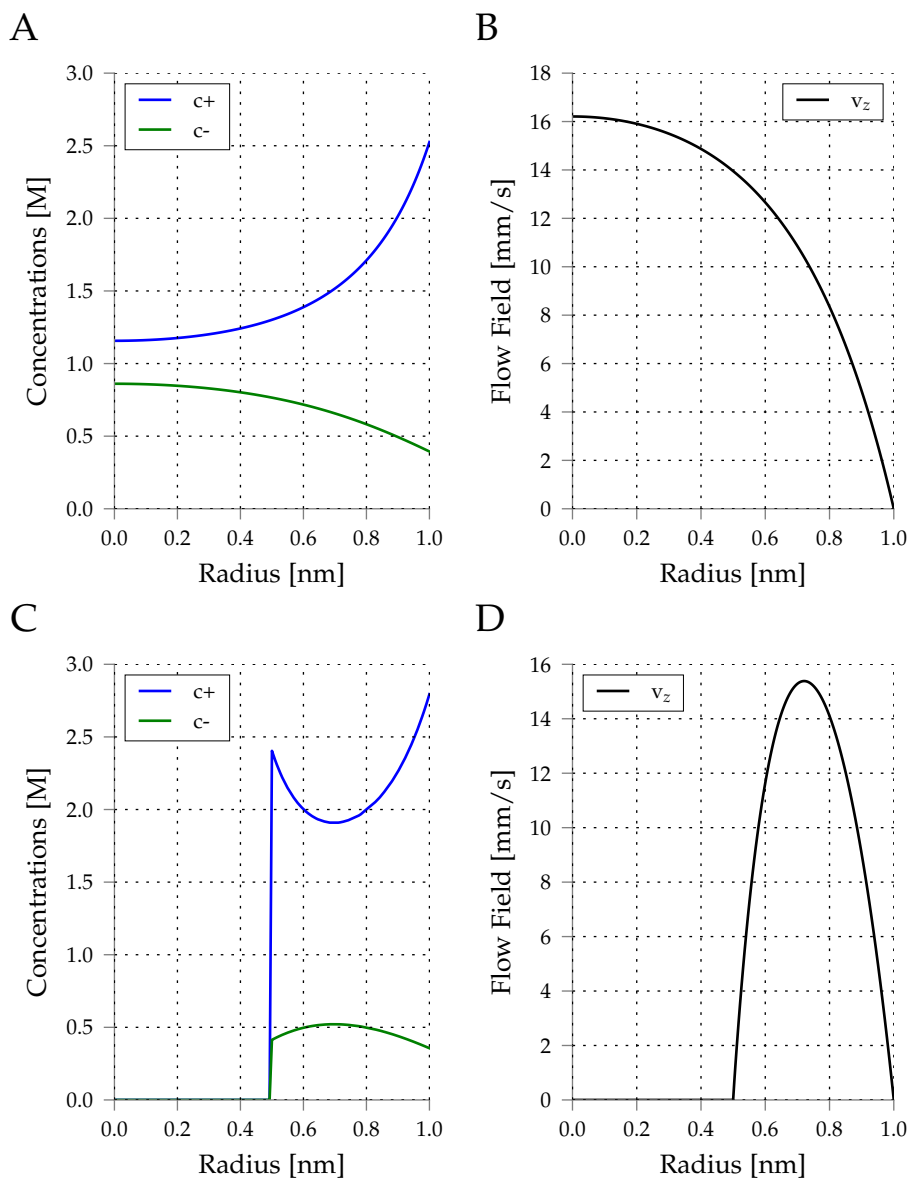
A

B

C

D

Figure 12: Concentrations and flow plotted for a cross-section of pore (P3) at the pore center. The variables are plotted over the radial distance from the rotational symmetry axis. The Debye length for this configuration amounts to 0.3 nm.
A. Concentrations of positive and negative ions inside an open pore. B. Vertical component of the fluid flow field inside an open pore. C. Concentrations of positive and negative ions inside a pore with a centered negatively charged 0.5 nm molecule. D. Vertical component of the fluid flow field inside a pore with a centered negatively charged 0.5 nm molecule.
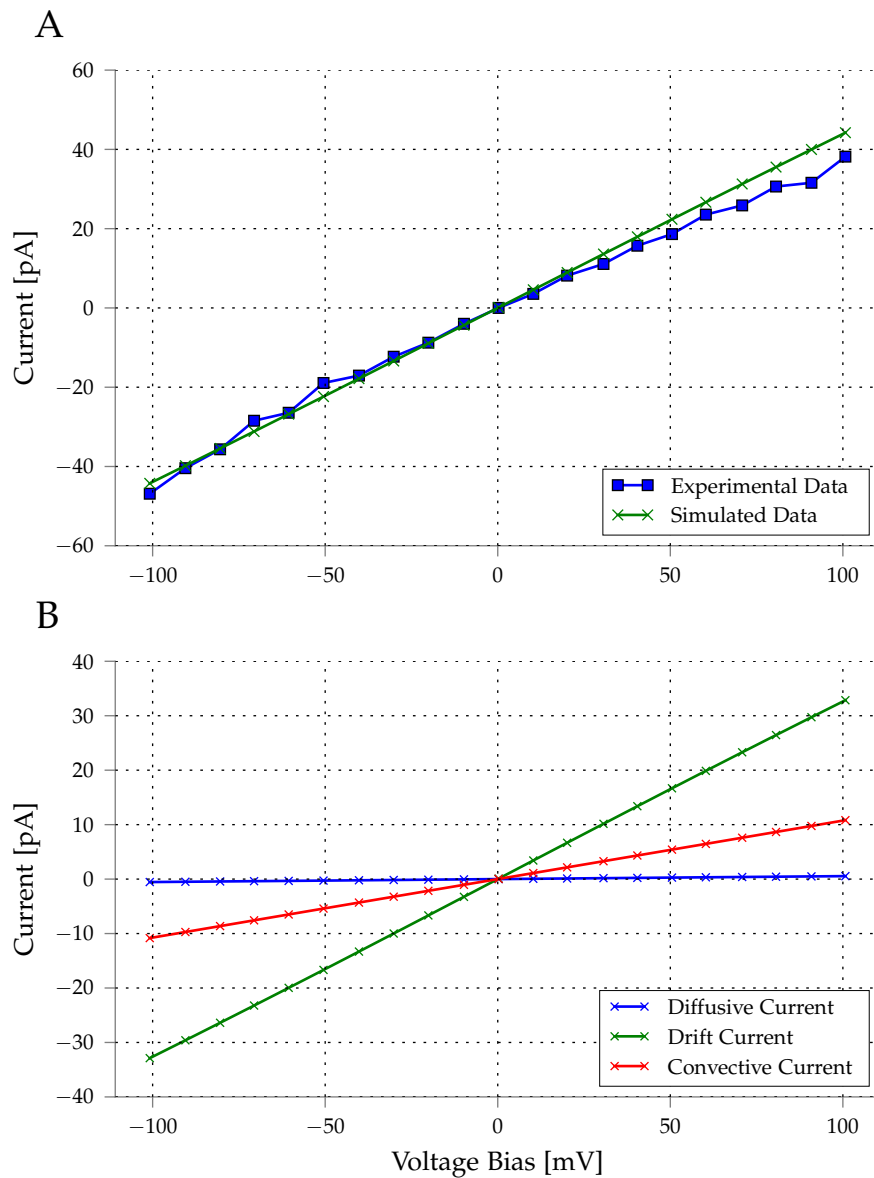
A

B

Figure 13: IV curve and current components for (P3). The diffusivity and DNA surface charge are reduced by 90% and 70% compared to their bulk values, respectively.

A. Comparison of the measured and simulated IV curve of (P3). The simulated IV curve is in good agreement with the experimental data. B. Current components over applied voltage for (P3). The diffusive current component (blue) is nearly zero, whereas there is a significant contribution from the Stokes current term (red) compared to the drift current (green).
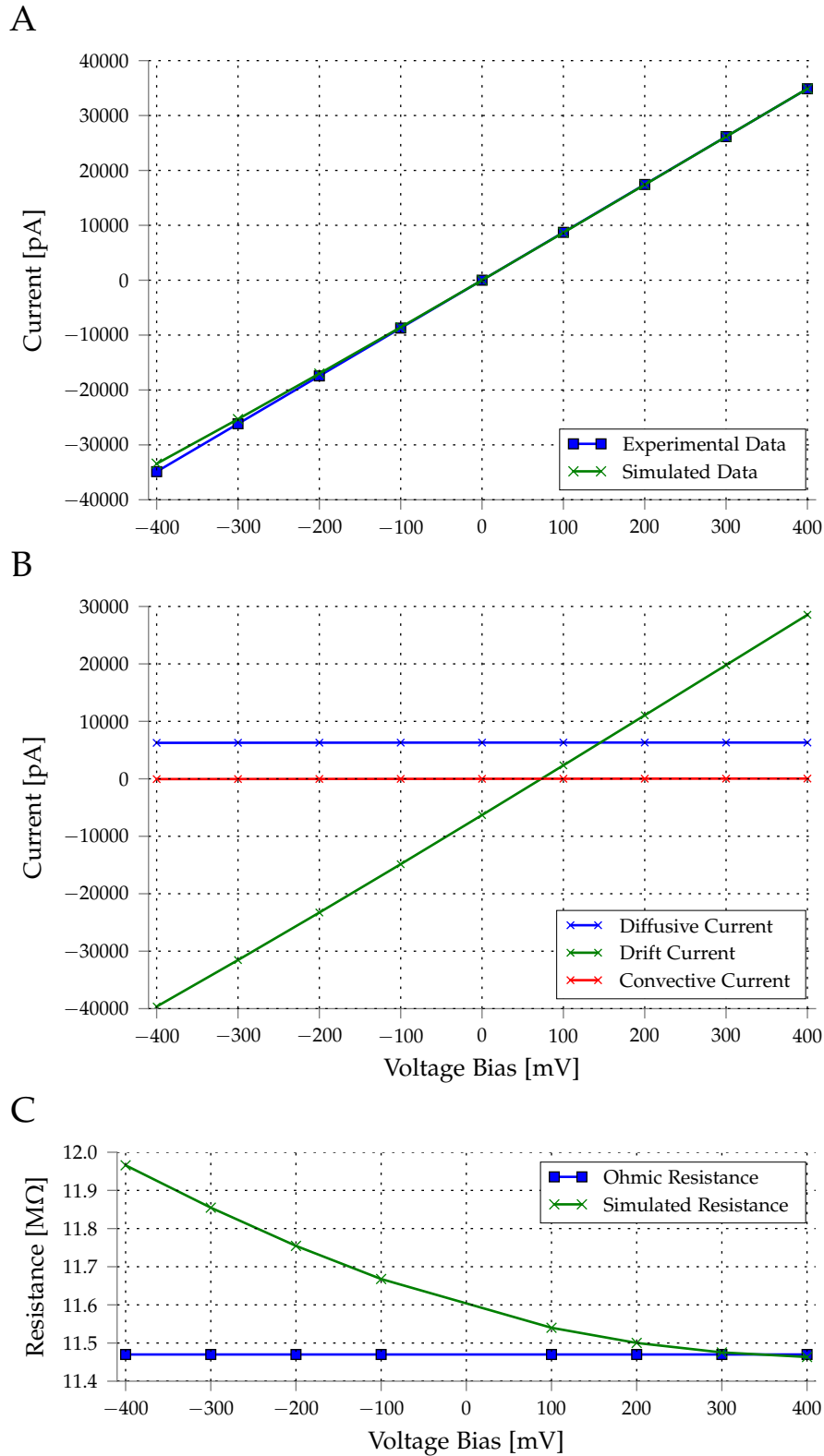
A

B

C

Figure 14: IV curve and current components and resistance for (P2).
A. Comparison of a simulated IV curve and a linear fit to
the experimentally measured resistance. B. Current com-
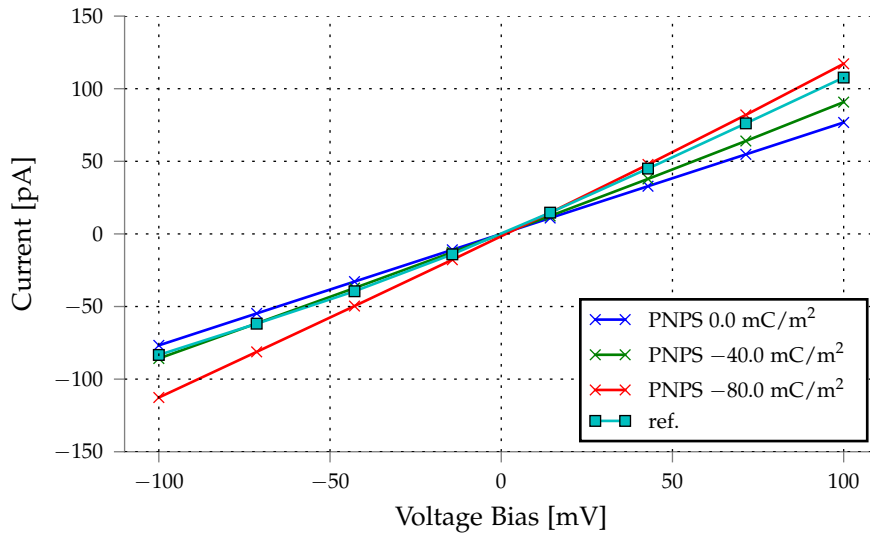ponents. C. Simulated against measured resistance.

Figure 15: IV curves for (P4) with a diffusivity of 0.475×10^{-9} m²/s and different surface charges inside the pore. IV curves simulated with the PNPS model are compared with the IV curve in [12].

conical shape. The asymmetry is stronger at higher voltages, as can be seen in Figure 14C.

Also, IV curves of the α-hemolysin pore (P4) were investigated. The results are shown in Figure 15. For the simulations behind this pore (P4), a bulk concentration of 1000 mM was used and the surface charge was varied. The diffusivity was reduced to 0.475×10^{-9} m²/s, i. e. to 25% of the bulk value. In [60], ionic flow through α-hemolysin is investigated with a PNP and a Brownian dynamics (BD) model. There, the diffusion constant was also lowered to around 70% of the bulk value depending on the cross-sectional area of the pore. Still, the PNP model in [60] overestimates the ion current.

The simulated IV curves were compared with the IV curve found in [12]. In [12], the current rectification in α-hemolysin pores was investigated for different cation types, as ICR is observed in the experiments. This feature could not be reproduced quantitatively, since only constant surface charges were used in the simulations. Clearly, an asymmetric surface charge inside the pore would yield better rectification properties.
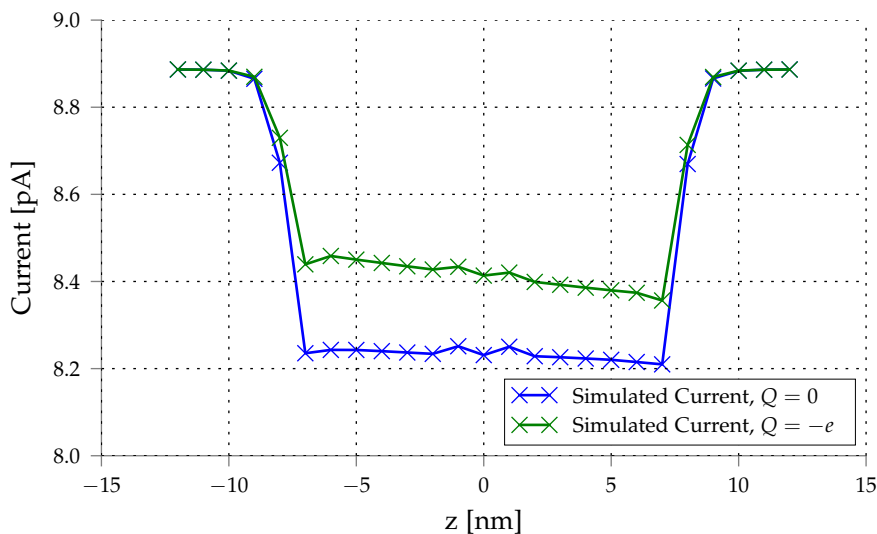
Figure 16: Current drop for a negatively charged molecule and an uncharged molecule along the axis of pore (P3).

4.6.3 Current Trace

In Figure 16 the current for varying molecule positions is shown. For both an uncharged and a charged molecule with radius 0.55 nm the current trace is displayed. The configuration of this simulation is chosen as specified in Section 4.4 for pore (P3). The current drop corresponds to the current difference between open and closed state. In this configuration, the current drop amounts to approximately 0.7 and 0.45 pA, respectively, as the open current is circa 8.9 pA.

4.6.4 Force Field

In this section, the force field for a 1.1 nm molecule is presented. The force field was calculated for pore (P3). For this simulation the setup was slightly different. There was no applied voltage across the pore; instead a concentration bias on the negative ions was applied. The molecule was negatively charged with valence -2, but the pore surface was assumed to be positive with surface charge 48 mC/m^2. One might think of the positive surface charge as a result of chemical modifications on the DNA or of overscreening of counterions. Thus, the negatively charged molecule is attracted to the pore wall. For a total number of nearly 2000 molecule positions the force was calculated. An interpolation of the obtained values can be seen in Figure 17. In Figure 17 the different forces in z-direction are plotted. As can be
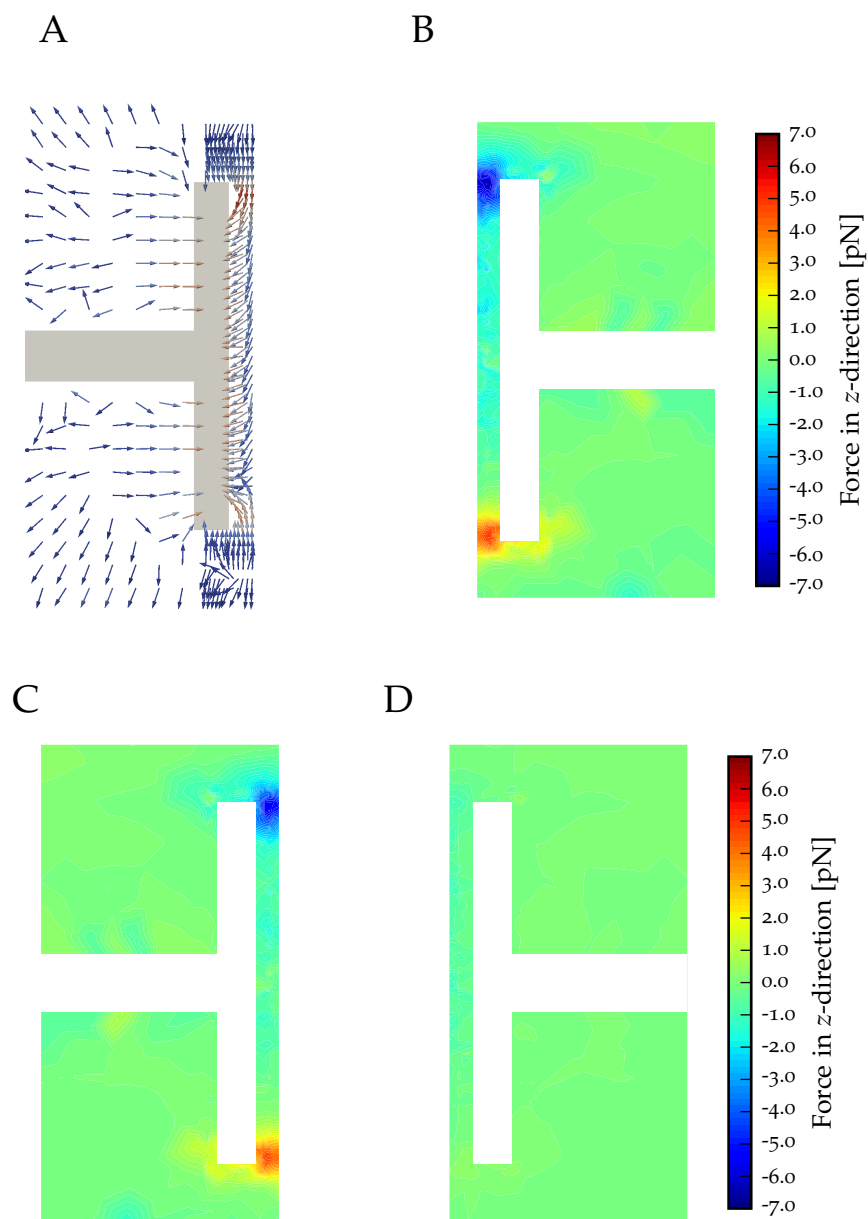
Figure 17: Force fields for pore (P3).
A. Effective force field. B. Effective force in vertical direction. C. Electric force in vertical direction. D. Drag force in vertical direction.

seen in the plots, the electric force is stronger than the drag force, thus the molecule is mainly driven by the electric force.

4.6.5   Comparison of Forces on Finite-Sized Molecules with Forces on Point-Like Molecules

In this section a comparison of the forces calculated by a simple model and the simulated forces is provided. The simple model assumes a point-like molecule, thus the forces are given by the electric force

$$F_{el} = -Q\nabla\phi(z_0) \tag{4.3}$$

and the Stokes drag

$$F_{drag} = \gamma_S\, v(z_0) \ . \tag{4.4}$$

Here $\gamma_S = 6\pi\eta r_{Mol}$ is the friction coefficient, r_{Mol} is the radius and z_0 is the midpoint of the molecule. The *Stokes-Einstein relation* for the diffusion coefficient reads

$$D = \frac{k_B T}{\gamma_S} \ . \tag{4.5}$$

Thus, if one combines (2.9) and (4.5), one finds that the mobility is inversely proportional to the friction coefficient.

Results are displayed in Figure 18 for the configuration specified in Section 4.4 for pore (P3). The simulations were restricted to the axisymmetric case, in the figures the x-axis represents the rotational symmetry axis z. Due to the axisymmetry only the vertical component of the forces is plotted. As already seen in the last section, the effective force is strongest at the opening, as shown in Figure 18A. In fact, there is a big barrier hindering the molecule from entering the pore. The electric force is in relatively good agreement with its simulated counterpart, cf. Figure 18C.

Figure 18B shows that the simulated drag force is approximately four times as big as the classic Stokes drag force. The results support the assumption of a lowered mobility inside the pore. In fact, a reduced molecule mobility corresponds to a higher friction coefficient and hence to a higher drag force. Edge effects at the pore openings are only captured by simulations with a macroscopic molecule. They can be observed for z-values between ± 6 and ± 8 nm.
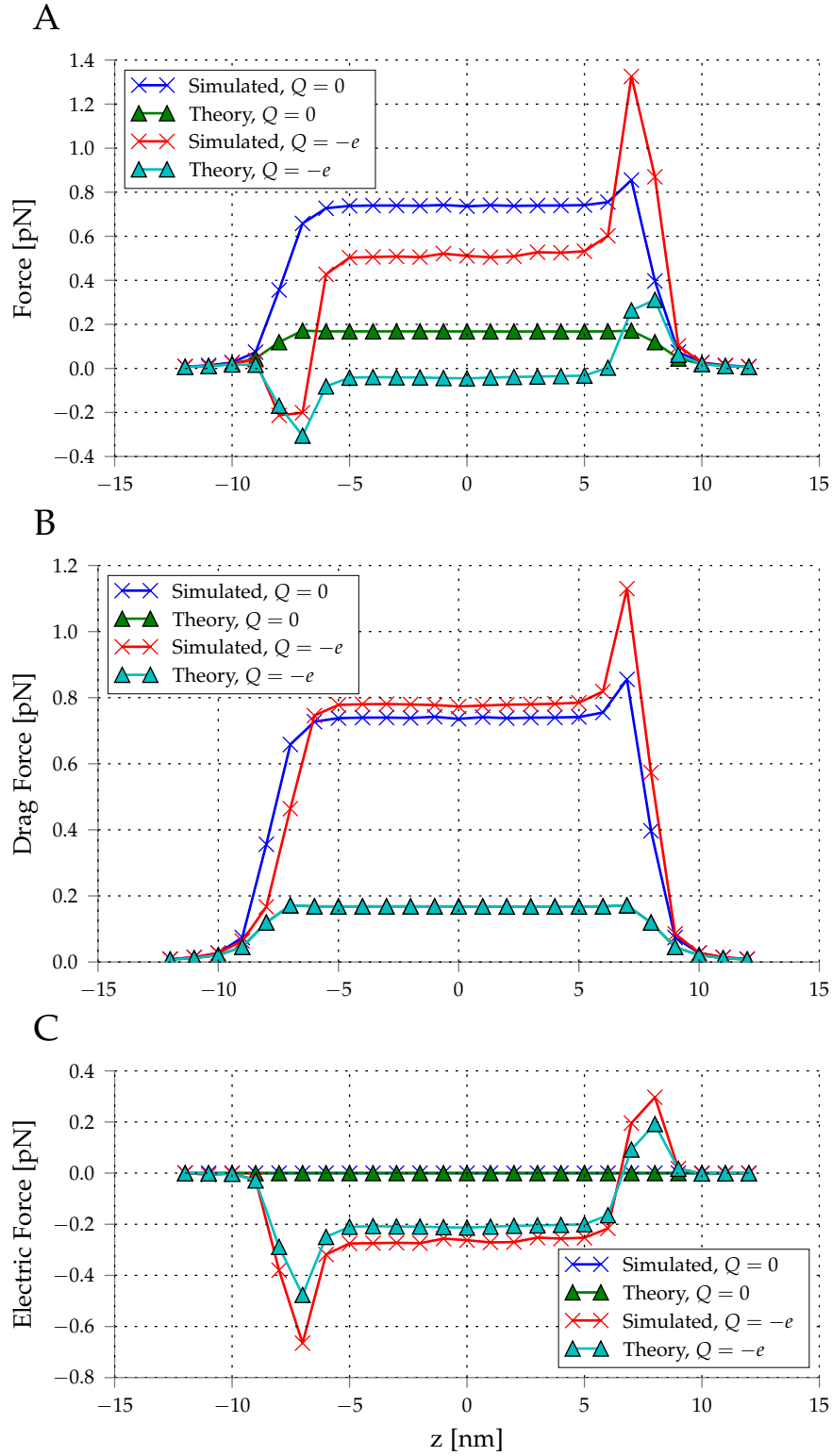
A

B

C

Figure 18: Forces acting on a molecule along the axis of pore (P3). Only the vertical force component is shown.
A. Effective force F_{eff}. B. Drag force F_{drag}. The values for the classic Stokes drag overlap. C. Electric force F_{el}.

CONCLUSION AND OUTLOOK

5

The overall goal of this thesis was twofold: The first task was the development of an efficient solver of the steady-state PNPS equations. The second task was to validate the modeling approach and to run simulation for different nanopore setups.

The numerical solver is based on a discretization of the PDE system by the method of finite elements (FEM). The first objective was resolved by a refinement of Newton's method and by adaptive mesh refinement. The efficiency of this approach regarding accuracy and computational effort was demonstrated. Still, full three dimensional simulations of big solid-state nanopores remain at the potential edge of today's workstations.

The simulations performed for four different nanopore setups gave valuable insight into the physics inside the pore. The computation of the effective driving force was verified with values given by a reference simulation. The model was validated by a conductance analysis for a DNA origami and a solid-state nanopore. Simulated IV curves were compared with experiments for those two pores as well as for the α-hemolysin pore. As the surface charge is not known exactly for most of the different nanopore setups, simulations with varying surface charge were run to clarify the influence of this parameter. Since only constant surface charges were used, the effects of ICR in α-hemolysin could not be completely reproduced. Therefore it might be interesting to implement non-constant surface charge densities. For the small DNA origami nanopore the upshot of the model validation was that the effective DNA charge and the ion mobility inside the pore have to be reduced.

Furthermore, in the case of the DNA origami nanopore the solvent flow had significant contributions to the calculation of the forces acting on molecules as well as to the current. For the large nanopore the effect of the solvent flow on the current was found to be negligible. After calibration of the parameters current-voltage curves were reproduced quantitatively. A calculated force field was shown to demonstrate the possibility of a comprehensible simulation of nanopores as stochastic sensors.

Another possible way of determining the forces acting on molecules would be to base the force calculations on accurate simulations with-

out finite-sized molecules as outlined in the last section of the previous chapter. Still, one would have to be careful with edge effects and physical parameters. Besides, as charges were only applied as constant surface or volume charges the force field may lack some features. For discrete ions one may expect the force field to have wells and springs, thus being not as uniform as in the performed simulations.

APPENDIX

PHYSICAL CONSTANTS AND PARAMETERS

In this section two tables containing the physical constants and the material parameters used in the simulations are provided.

Table 4: Fundamental physical constants

Symbol	Constant	Value	Unit
e	elementary charge	1.602×10^{-19}	C
N_A	Avogadro constant	6.022×10^{23}	mol^{-1}
k_B	Boltzmann constant	1.381×10^{-23}	J K^{-1}
ϵ_0	vacuum permittivity	8.854×10^{-12}	$\text{C V}^{-1} \text{m}^{-1}$
F	Faraday constant	$96\,485 = eN_A$	C mol^{-1}

Table 5: Material parameters

Symbol	Parameter	Value	Unit
μ	bulk ion mobility of K^+, Cl^-	73×10^{-9}	m^2/Vs
η	fluid viscosity	1×10^{-3}	kg/m/s
ρ	fluid density	1×10^3	kg/m^3
D	bulk diffusivity of K^+, Cl^-	1.9×10^{-9}	m^2/s
ϵ_L	relative permittivity of the lipid bilayer	2.0	1
ϵ_{DNA}	relative permittivity of dsDNA	12.0 [a]	1
ϵ_{SAM}	relative permittivity of SAM	2.7 [b]	1
ϵ_{Au}	relative permittivity of gold	6.9	1
T	temperature	293	K

[a] according to [29]
[b] according to [70]

BIBLIOGRAPHY

[1] R. A. Adams. *Sobolev Spaces*. Pure and Applied Mathematics, Vol. 65. Academic Press, New York-London, 1975, pp. xviii+268 (cit. on p. 14).

[2] Y. Ai, M. Zhang, S. W. Joo, M. A. Cheney, and S. Qian. Effects of electroosmotic flow on ionic current rectification in conical nanopores. *The Journal of Physical Chemistry C* 114.9 (2010), pp. 3883–3890. DOI: 10.1021/jp911773m (cit. on p. 2).

[3] M. S. Alnæs. UFL: a finite element form language. *Automated Solution of Differential Equations by the Finite Element Method, Volume 84 of Lecture Notes in Computational Science and Engineering*. Springer, 2012. Chap. 17 (cit. on p. 34).

[4] M. S. Alnæs, A. Logg, and K.-A. Mardal. UFC: a finite element code generation interface. *Automated Solution of Differential Equations by the Finite Element Method, Volume 84 of Lecture Notes in Computational Science and Engineering*. Springer, 2012. Chap. 16 (cit. on p. 34).

[5] M. S. Alnæs and K.-A. Mardal. SyFi and SFC: symbolic finite elements and form compilation. *Automated Solution of Differential Equations by the Finite Element Method, Volume 84 of Lecture Notes in Computational Science and Engineering*. Springer, 2012. Chap. 15 (cit. on p. 34).

[6] P. Y. Apel, Y. E. Korchev, Z. Siwy, R. Spohr, and M. Yoshida. Diode-like single-ion track membrane prepared by electro-stopping. *Nuclear Instruments and Methods in Physics Research Section B: Beam Interactions with Materials and Atoms* 184.3 (2001), pp. 337–346 (cit. on p. 9).

[7] M. Ayub, S. W. Hardwick, B. F. Luisi, and H. Bayley. Nanopore-based identification of individual nucleotides for direct RNA sequencing. *Nano Letters* 13 (2013), pp. 6144 –6150. DOI: 10.1021/nl403469r (cit. on pp. 1, 35).

[8] W. Bangerth and R. Rannacher. *Adaptive Finite Element Methods for Differential Equations*. Lectures in Mathematics ETH Zürich. Birkhäuser Verlag, Basel, 2003, pp. viii+207. DOI: 10.1007/978-3-0348-7605-6 (cit. on pp. 26–28, 30, 31).

[9]   H. Bayley and P. S. Cremer. Stochastic sensors inspired by biology. *Nature* 413.6852 (2001), pp. 226–230 (cit. on p. 1).

[10] S. H. Behrens and D. G. Grier. The charge of glass and silica surfaces. *The Journal of Chemical Physics* 115.14 (2001), pp. 6716–6721 (cit. on p. 39).

[11] N. A. W. Bell, C. R. Engst, M. Ablay, G. Divitini, C. Ducati, T. Liedl, and U. F. Keyser. DNA origami nanopores. *Nano Letters* 12.1 (2012), pp. 512–517. DOI: 10.1021/nl204098n (cit. on pp. 1, 2).

[12] S. Bhattacharya, J. Muzard, L. Payet, J. Mathé, U. Bockelmann, A. Aksimentiev, and V. Viasnoff. Rectification of the current in α-hemolysin pore depends on the cation type: the alkali series probed by molecular dynamics simulations and experiments. *The Journal of Physical Chemistry C* 115.10 (2011), pp. 4255–4264. DOI: 10.1021/jp111441p (cit. on p. 51).

[13] S. C. Brenner and L. R. Scott. *The Mathematical Theory of Finite Element Methods*. Texts in applied mathematics ; 15. New York, NY [u.a.]: Springer, 1996 (cit. on pp. 13–15, 22–24).

[14] J. R. Burns, E. Stulz, and S. Howorka. Self-assembled DNA nanopores that span lipid bilayers. *Nano Letters* 13.6 (2013), pp. 2351 –2356. DOI: 10.1021/nl304147f (cit. on pp. 2, 35, 37, 41).

[15] A. Castellanos. *Electrohydrodynamics*. CISM International Centre for Mechanical Sciences. Springer Vienna, 2014 (cit. on p. 7).

[16] J. H. Chaudhry, J. Comer, A. Aksimentiev, and L. N. Olson. A stabilized finite element method for modified Poisson-Nernst-Planck equations to determine ion flow through a nanopore. *Communications in Computational Physics* 15.1 (2014) (cit. on p. 40).

[17] L. Chen, M. J. Holst, and J. Xu. The finite element approximation of the nonlinear Poisson-Boltzmann equation. *SIAM Journal on Numerical Analysis* 45.6 (2007), pp. 2298–2320. DOI: 10.1137/060675514 (cit. on p. 17).

[18] J. Clarke, H.-C. Wu, L. Jayasinghe, A. Patel, S. Reid, and H. Bayley. Continuous base identification for single-molecule nanopore DNA sequencing. *Nature Nanotechnology* 4.4 (Apr. 2009), pp. 265–270. DOI: 10.1038/nnano.2009.12 (cit. on p. 1).

[19] B. Corry, S. Kuyucak, and S. Chung. Invalidity of continuum theories of electrolytes in nanopores. *Chemical Physics Letters* 320.1–2 (2000), pp. 35 –41. DOI: 10.1016/S0009-2614(00)00206-2 (cit. on p. 40).

[20] B. Corry, S. Kuyucak, and S.-H. Chung. Dielectric self-energy in Poisson-Boltzmann and Poisson-Nernst-Planck models of ion channels. *Biophysical Journal* 84.6 (2003), pp. 3594 –3606. DOI: 10.1016/S0006-3495(03)75091-7 (cit. on p. 40).

[21] J. A. Cracknell, D. Japrung, and H. Bayley. Translocating kilobase RNA through the staphylococcal α-hemolysin nanopore. *Nano Letters* 13.6 (2013), pp. 2500–2505. DOI: 10.1021/nl400560r (cit. on p. 1).

[22] E. R. Cruz-Chu, A. Aksimentiev, and K. Schulten. Ionic current rectification through silica nanopores. *The Journal of Physical Chemistry C, Nanomaterials and Interfaces* 113.5 (Feb. 2009), p. 1850. DOI: 10.1021/jp804724p (cit. on p. 2).

[23] H. Daiguji. Ion transport in nanofluidic channels. *Chemical Society Reviews* 39 (3 2010), pp. 901–911. DOI: 10.1039/B820556F (cit. on p. 2).

[24] V. Debye and E. Hückel. Zur Theorie der Elektrolyte. *Physikalische Zeitschrift* 24.9 (1923), pp. 185–206 (cit. on p. 11).

[25] S. Deparis. Numerical analysis of axisymmetric flows and methods for fluid-structure interaction arising in blood flow simulation. PhD thesis. École Polytechnique Fédérale de Lausanne, 2004 (cit. on p. 26).

[26] S. van Dorp, U. F. Keyser, N. H. Dekker, C. Dekker, and S. G. Lemay. Origin of the electrophoretic force on DNA in solid-state nanopores. *Nature Physics* 5.5 (May 2009), pp. 347–351. DOI: 10.1038/nphys1230 (cit. on p. 2).

[27] H. C. Elman, D. J. Silvester, and A. J. Wathen. *Finite Elements and Fast Iterative Solvers: with Applications in Incompressible Fluid Dynamics*. Numerical Mathematics and Scientific Computation. Oxford University Press, Oxford, 2014, pp. xiv+479. DOI: 10.1093/acprof:oso/9780199678792.001.0001 (cit. on pp. 23, 24, 33).

[28] M. Firnkes, D. Pedone, J. Knezevic, M. Döblinger, and U. Rant. Electrically facilitated translocations of proteins through silicon nitride nanopores: conjoint and competitive action of diffusion, electrophoresis, and electroosmosis. *Nano Letters* 10.6 (2010), pp. 2162–2167. DOI: 10.1021/nl100861c (cit. on p. 39).

[29] L. Fumagalli, D. Esteban-Ferrer, A. Cuervo, J. L. Carrascosa, and G. Gomila. Label-free identification of single dielectric nanoparticles and viruses with ultraweak polarization forces. *Nature Materials* 11.9 (Sept. 2012), pp. 808–816. DOI: 10.1038/nmat3369 (cit. on p. 59).

[30] C. Geuzaine and J.-F. Remacle. Gmsh: A 3-D finite element mesh generator with built-in pre- and post-processing facilities. *International Journal for Numerical Methods in Engineering* 79.11 (2009), pp. 1309–1331. DOI: `10.1002/nme.2579` (cit. on p. 34).

[31] M. S. Gockenbach. *Understanding and Implementing the Finite Element Method*. Society for Industrial and Applied Mathematics (SIAM), Philadelphia, PA, 2006, pp. xvi+363. DOI: `10.1137/1.9780898717846` (cit. on pp. 13, 33).

[32] F. Haque, J. Li, H.-C. Wu, X.-J. Liang, and P. Guo. Solid-state and biological nanopore for real-time sensing of single chemical and sequencing of DNA. *Nano Today* 8.1 (2013), pp. 56–74 (cit. on p. 2).

[33] C. Heitzinger and C. Ringhofer. A transport equation for confined structures derived from the Boltzmann equation. *Communications in Mathematical Sciences* 9.3 (2011), pp. 829 –857 (cit. on p. 40).

[34] C. Heitzinger and C. Ringhofer. Hierarchies of transport equations for nanopores. *Journal of Computational Electronics* 13.4 (2014), pp. 801–817. DOI: `10.1007/s10825-014-0586-8` (cit. on pp. 3, 6, 40).

[35] J. G. Heywood, R. Rannacher, and S. Turek. Artificial boundaries and flux and pressure conditions for the incompressible Navier-Stokes equations. *International Journal for Numerical Methods in Fluids* 22.5 (1996), pp. 325–352. DOI: `10.1002/(SICI)1097-0363(19960315)22:5<325::AID-FLD307>3.0.CO;2-Y` (cit. on p. 10).

[36] C. Ho, R. Qiao, J. B. Heng, A. Chatterjee, R. J. Timp, N. R. Aluru, and G. Timp. Electrolytic transport through a synthetic nanometer-diameter pore. *Proceedings of the National Academy of Sciences* 102.30 (July 2005), pp. 10445–10450. DOI: `10.1073/pnas.0500796102` (cit. on pp. 8, 41, 43).

[37] M. Holst, J. A. Mccammon, Z. Yu, Y. Zhou, and Y. Zhu. Adaptive finite element modeling techniques for the Poisson-Boltzmann equation. *Communications in computational physics* 11.1 (2012), p. 179 (cit. on p. 17).

[38] S. Howorka and Z. Siwy. Nanopore analytics: sensing of single molecules. *Chemical Society Reviews* 38 (2009), pp. 2360 –2384. DOI: `10.1039/B813796J` (cit. on p. 2).

[39]   K. Hu and A. J. Bard. Use of atomic force microscopy for the study of surface acid-base properties of carboxylic acid-terminated self-assembled monolayers. *Langmuir* 13.19 (1997), pp. 5114 –5119 (cit. on p. 38).

[40]   T. Z. Jubery, A. S. Prabhu, M. J. Kim, and P. Dutta. Modeling and simulation of nanoparticle separation through a solid-state nanopore. *Electrophoresis* 33.2 (2012), pp. 325–333. DOI: 10.1002/elps.201100201 (cit. on p. 3).

[41]   J. J. Kasianowicz, E. Brandin, D. Branton, and D. W. Deamer. Characterization of individual polynucleotide molecules using a membrane channel. *Proceedings of the National Academy of Sciences* 93.24 (1996), pp. 13770–13773 (cit. on p. 1).

[42]   U. F. Keyser, B. N. Koeleman, S. van Dorp, D. Krapf, R. M. M. Smeets, S. G. Lemay, N. H. Dekker, and C. Dekker. Direct force measurements on DNA in a solid-state nanopore. *Nature Physics* 2 (2006), pp. 473–477. DOI: 10.1038/nphys344 (cit. on p. 41).

[43]   M. S. Kilic, M. Z. Bazant, and A. Ajdari. Steric effects in the dynamics of electrolytes at large applied voltages. I. Double-layer charging. *Physical Reviews E* 75 (2 Feb. 2007), p. 021502. DOI: 10.1103/PhysRevE.75.021502 (cit. on p. 40).

[44]   M. S. Kilic, M. Z. Bazant, and A. Ajdari. Steric effects in the dynamics of electrolytes at large applied voltages. II. Modified Poisson-Nernst-Planck equations. *Physical Reviews E* 75 (2 Feb. 2007), p. 021503. DOI: 10.1103/PhysRevE.75.021503 (cit. on p. 40).

[45]   R. C. Kirby. FIAT: numerical construction of finite element basis functions. *Automated Solution of Differential Equations by the Finite Element Method, Volume 84 of Lecture Notes in Computational Science and Engineering*. Springer, 2012. Chap. 13 (cit. on p. 34).

[46]   M. Langecker, V. Arnaut, T. G. Martin, J. List, S. Renner, M. Mayer, H. Dietz, and F. C. Simmel. Synthetic lipid membrane channels formed by designed DNA nanostructures. *Science* 338.6109 (2012), pp. 932–936. DOI: 10.1126/science.1225624 (cit. on p. 2).

[47]   N. Laohakunakorn and U. F. Keyser. Electroosmotic flow rectification in conical nanopores. *Nanotechnology* 26.27 (2015), p. 275202 (cit. on p. 2).

[48]   M. G. Larson and F. Bengzon. *The Finite Element Method: Theory, Implementation, and Applications*. Vol. 10. Texts in Computational Science and Engineering. Springer, Heidelberg, 2013, pp. xviii+385. DOI: 10.1007/978-3-642-33287-6 (cit. on pp. 10, 13, 14, 21, 22, 25).

[49]   J. Liu, M. Kvetny, J. Feng, D. Wang, B. Wu, W. Brown, and G. Wang. Surface charge density determination of single conical nanopores based on normalized ion current rectification. *Langmuir* 28.2 (2012), pp. 1588–1595. DOI: 10.1021/la203106 (cit. on p. 2).

[50]   A. Logg, K.-A. Mardal, G. N. Wells, et al. *Automated Solution of Differential Equations by the Finite Element Method*. Springer, 2012. DOI: 10.1007/978-3-642-23099-8 (cit. on pp. 13, 34).

[51]   A. Logg, G. N. Wells, and J. Hake. DOLFIN: a C++/Python finite element library. *Automated Solution of Differential Equations by the Finite Element Method, Volume 84 of Lecture Notes in Computational Science and Engineering*. Springer, 2012. Chap. 10 (cit. on p. 34).

[52]   A. Logg, K. B. Ølgaard, M. E. Rognes, and G. N. Wells. FFC: the FEniCS form compiler. *Automated Solution of Differential Equations by the Finite Element Method, Volume 84 of Lecture Notes in Computational Science and Engineering*. Springer, 2012. Chap. 11 (cit. on p. 34).

[53]   B. Lu, M. J. Holst, J. A. McCammon, and Y. C. Zhou. Poisson-Nernst-Planck equations for simulating biomolecular diffusion-reaction processes I: finite element solutions. *Journal of Computational Physics* 229.19 (2010), pp. 6979 –6994 (cit. on p. 17).

[54]   B. Lu, D. P. Hoogerheide, Q. Zhao, and D. Yu. Effective driving force applied on DNA inside a solid-state nanopore. *Physical Reviews E* 86 (1 July 2012), p. 011921. DOI: 10.1103/PhysRevE.86.011921 (cit. on pp. 2, 9, 35, 37, 39, 43, 45).

[55]   C. Maffeo, S. Bhattacharya, J. Yoo, D. Wells, and A. Aksimentiev. Modeling and simulation of ion channels. *Chemical Reviews* 112.12 (2012), pp. 6250–6284. DOI: 10.1021/cr3002609 (cit. on pp. 2, 40).

[56]   M. Mao, S. Ghosal, and G. Hu. Hydrodynamic flow in the vicinity of a nanopore induced by an applied voltage. *Nanotechnology* 24.24 (2013), p. 245202 (cit. on pp. 2, 41, 47).

[57]   B. N. Miles, A. P. Ivanov, K. A. Wilson, F. Doğan, D. Japrung, and J. B. Edel. Single molecule sensing with solid-state nanopores: novel materials, methods, and applications. *Chemical Society Reviews* 42.1 (2013), pp. 15–28 (cit. on p. 2).

[58]   G. Mitscha-Eibl, A. Buttinger-Kreuzhuber, G. Tulzer, and C. Heitzinger. Nonlinear coupling of the drift-diffusion-Poisson and Stokes systems for nanopore simulations. *Proceedings of the 13th US National Congress on Computational Mechanics*. San Diego CA, USA, July 2015 (cit. on p. 1).

[59]   B. Nadler, Z. Schuss, A. Singer, and R. S. Eisenberg. Ionic diffusion through confined geometries: from Langevin equations to partial differential equations. *Journal of Physics: Condensed Matter* 16.22 (2004), S2153 (cit. on pp. 5, 40).

[60]   S. Y. Noskov, W. Im, and B. Roux. Ion permeation through the α-hemolysin channel: theoretical studies based on Brownian dynamics and Poisson-Nernst-Planck electrodiffusion theory. *Biophysical Journal* 87.4 (2004), pp. 2299–2309 (cit. on p. 51).

[61]   K. Pratt, W. Koch, Y. Wu, and P. Berezansky. Molality-based primary standards of electrolytic conductivity (IUPAC Technical Report). *Pure and Applied Chemistry* 73.11 (2001), pp. 1783–1793 (cit. on p. 39).

[62]   M. E. Rognes and A. Logg. Automated goal-oriented error control I: Stationary variational problems. *SIAM Journal on Scientific Computing* 35.3 (2013), pp. C173–C193. DOI: 10.1137/10081962X (cit. on pp. 28–30).

[63]   Y. Saad. *Iterative Methods for Sparse Linear Systems*. Society for Industrial and Applied Mathematics, Philadelphia, PA, 2003, pp. xviii+528. DOI: 10.1137/1.9780898718003 (cit. on p. 33).

[64]   M. Schmuck. Analysis of the Navier-Stokes-Nernst-Planck-Poisson system. *Mathematical Models and Methods in Applied Sciences* 19.6 (2009), pp. 993–1015. DOI: 10.1142/S0218202509003693 (cit. on p. 7).

[65]   A. Seifert, K. Göpfrich, J. R. Burns, N. Fertig, U. F. Keyser, and S. Howorka. Bilayer-spanning DNA nanopores with voltage-switching between open and closed state. *ACS Nano* 9.2 (2015), pp. 1117–1126. DOI: 10.1021/nn5039433 (cit. on pp. 2, 41).

[66]   Z. Siwy. Ion-current rectification in nanopores and nanotubes with broken symmetry. *Advanced Functional Materials* 16.6 (2006), pp. 735–746. DOI: 10.1002/adfm.200500471 (cit. on p. 2).

[67] R. M. M. Smeets, U. F. Keyser, D. Krapf, M.-Y. Wu, N. H. Dekker, and C. Dekker. Salt dependence of ion transport and DNA translocation through solid-state nanopores. *Nano Letters* 6.1 (2006), pp. 89–95 (cit. on pp. 39, 41).

[68] L. Song, M. R. Hobaugh, C. Shustak, S. Cheley, H. Bayley, and J. E. Gouaux. Structure of staphylococcal α-hemolysin, a heptameric transmembrane pore. *Science* 274.5294 (1996), pp. 1859–1865. DOI: `10.1126/science.274.5294.1859` (cit. on p. 35).

[69] B. M. Venkatesan and R. Bashir. Nanopore sensors for nucleic acid analysis. *Nature Nanotechnology* 6.10 (2011), pp. 615–624 (cit. on p. 2).

[70] R. Wei, V. Gatterdam, R. Wieneke, R. Tampe, and U. Rant. Stochastic sensing of proteins with receptor-modified solid-state nanopores. *Nature Nanotechnology* 7.4 (Apr. 2012), pp. 257–263. DOI: `10.1038/nnano.2012.24` (cit. on pp. 1, 35, 37, 43, 44, 47, 59).

[71] H. S. White, and A. Bund. Ion current rectification at nanopores in glass membranes. *Langmuir* 24.5 (2008), pp. 2212–2218. DOI: `10.1021/la702955k` (cit. on p. 2).

[72] J. M. Xue, X. Q. Zou, Y. B. Xie, and Y. G. Wang. Molecular dynamics simulations on the ionic current through charged nanopores. *Journal of Physics D: Applied Physics* 42.10 (2009), p. 105308 (cit. on pp. 2, 43).